minerals

MDPI

Article

Formation of Esseneite and Kushiroite in Tschermakite-Bearing Calc-Silicate Xenoliths Ejected in Alkali Basalt

Luca Reato [1], Monika Huraiová [1], Patrik Konečný [2], František Marko [3] and Vratislav Hurai [4,*]

[1] Department of Mineralogy, Petrology and Economic Geology, Faculty of Natural Sciences, Comenius University, Ilkovičova 6, 842 15 Bratislava, Slovakia; reato1@uniba.sk (L.R.); monika.huraiova@uniba.sk (M.H.)
[2] Department of Special Laboratories, State Geological Institute of Dionýz Štúr, Mlynská Dolina 1, 817 04 Bratislava, Slovakia; patrik.konecny@geology.sk
[3] Department of Geology and Paleontology, Faculty of Natural Sciences, Comenius University, Ilkovičova 6, 842 15 Bratislava, Slovakia; frantisek.marko@uniba.sk
[4] Institute of Earth Sciences, Slovak Academy of Sciences, Dúbravská Cesta 9, 840 05 Bratislava, Slovakia
* Correspondence: vratislav.hurai@savba.sk; Tel.: +421-2-32293209

Abstract: Skarnoid calc-silicate xenoliths composed of anorthite, clinopyroxene and Mg-Al spinel occur in alkali basalts of the Pliocene-Pleistocene intra-plate magmatic province in the northern part of the Pannonian Basin. Randomly oriented and elongated pseudomorphs are tschermakite crystals replaced by olivine, spinel and plagioclase. The relict amphibole within the pseudomorphs is characterized by high ^{VI}Al, between 1.95 and 2.1, and very low occupancy of the A-site (<0.1 apfu)—these features are rarely found in nature and are thought to be diagnostic of high-pressure metamorphic rocks. Pyroxene compositions plot along continuous mixing line extending from nearly pure diopside-augite towards a Ca(Fe^{3+}Al)$AlSiO_6$ endmember with an equal proportion of $^{VI}Al^{3+}$ and Fe^{3+}. Concentrations of kushiroite $CaAlAlSiO_6$ endmember, up to 47.5 mol%, are the highest recorded in terrestrial samples. The $AlFe^{3+}$-rich pyroxenes originated at the expense of diopside-augite during the interaction with carbonate-aluminosilicate melt. Forsterite ($Fo_{72–83}$) and hemoilmenite with up to 32 mol% geikielite (9.3 wt% MgO) also crystallized from the melt, leaving behind the residual calcic carbonate with minor MgO (1–3 wt%). Columnar habit of neoformed olivine growing across diopside-augite layers indicates rapid crystallization from eutectic liquid. Euhedral aragonite and apatite embedded in fine-grained calcite or aragonite groundmass indicate slow crystallization of the residual carbonatite around the calcite-aragonite stability boundary. Corundum exsolutions in rock-forming anorthite are products of superimposed low-pressure pyrometamorphic reworking during transport in alkali basalt. Concomitant alkali metasomatism produced neoformed interstitial sodalite, nepheline, sanidine, albite, biotite, Mg-poor ilmenite (10–18 mol% $MgTiO_3$), Ti-magnetite and fluorapatite. Olivine-ilmenite-aragonite-calcite thermobarometry returned temperatures of 770–860 °C and pressures of 1.8–2.1 GPa, whereas plagioclase-amphibole thermobarometer yielded 781 ± 13 °C and 2.05 ± 0.03 GPa. The calculated pressures correspond to depths of 60–70 km. The calc-silicate xenoliths are most likely metamorphosed marbles; however, a magmatic protolith (metagabbro, metaanorthosite) cannot be ruled out owing to high Cr contents in spinels (up to 30 mol% chromite) and abundant Cu-sulfides.

Keywords: xenolith; kushiroite; esseneite; melilite; alkali basalt; Carpathians

check for updates

Citation: Reato, L.; Huraiová, M.; Konečný, P.; Marko, F.; Hurai, V. Formation of Esseneite and Kushiroite in Tschermakite-Bearing Calc-Silicate Xenoliths Ejected in Alkali Basalt. *Minerals* **2022**, *12*, 156. https://doi.org/10.3390/min12020156

Academic Editors: Antonio Langone, Maria Pia Riccardi and Mattia Bonazzi

Received: 31 December 2021
Accepted: 25 January 2022
Published: 27 January 2022

Publisher's Note: MDPI stays neutral with regard to jurisdictional claims in published maps and institutional affiliations.

1. Introduction

Esseneite is a rare mineral of the pyroxene group with an ideal formula $CaFe^{3+}AlSiO_6$, which has been for the first time described from pyrometamorphic rocks (paralavas), i.e., fused sedimentary rock adjacent to naturally burned coal seams [1]. It is named in honor of Eric J. Essene, metamorphic petrologist and Professor of Geology at the University of Michigan, who discovered the first specimen. Mineral assemblages in the paralavas

from the type locality (Durham ranch in the Powder River Basin, WY, USA) are locally silica-undersaturated, and the esseneite is here associated with melilite, anorthite, solid solution of magnetite-hercynite and glass. In the same year, Ca-clinopyroxene with a very high amount of Fe and Al was described in buchite from Wyoming [2]. The slag-resembling buchite originated from near-surface combustion of the coal seam. During this process, underlying sequences of sandstones, siltstones and shales were heated and partially fused. Beside the Fe^{3+}-rich clinopyroxene, Fe^{3+}-rich melilites and oxides have also been produced. Slags like buchite, but devoid of glass, have also been discovered in bituminous shales intercalated with limestones and lignites from the Lapanouse-de-Sévérac area in France [3]. Here, unusual clinopyroxenes of mostly diopsidic composition, with a high content of esseneite molecule (up to 20 mol%), coexisting with wollastonite and leucite were formed during natural combustion. Clinopyroxenes with high Fe^{3+} and Al were also described in burnt dumps of coal pits in the Chelyabinsk and Kizel coal basins of the Urals [4]. Up to 51 mol% esseneite was determined in clinopyroxenes from hydrogarnet-zeolite-calcite rocks associated with paralavas of the Hatrurim basin, Israel, originating by the burning of hydrocarbon gas ejecta [5]. Esseneite is therefore considered predominantly a high-temperature product originating in strongly oxidizing conditions in natural or anthropogenic places of coal burning. Recent studies also proved the magmatic origin of esseneite. Oxidizing conditions and high temperatures derived from the crystal structure of esseneite were reported from ultramafic xenoliths in dacite flow of the Ten'-01 paleovolcano at the Lena–Vilyui watershed, East Yakutia [6]. Exceptional is the occurrence of esseneite and Ca-Tschermak component-dominated pyroxenes in Ciclova and Magureaua Vat ei skarns, Romania [7], where both pyroxene types occur in veinlets or inclusions in calcite and wollastonite close to the contact of marble with monzodioritic intrusions. The pyroxenes are interpreted here as remnants of high-temperature pyrometamorphism of early magmatic mineralization overprinted by post-magmatic processes. Extremely high content of Al in the Ca-pyroxene is concentrated in Ca-Tschermak's molecule.

Kushiroite, $CaAlAlSiO_6$, is nearly pure aluminian analogue of esseneite firstly discovered in a refractory inclusion of the CH-group carbonaceous chondrite ALH 85085. The mineral initially described as Ca-Tschermak-rich (CaTs) pyroxene [8] was later approved and renamed in honor of Ikuo Kushiro, Professor Emeritus at the University of Tokyo, Japan [9]. Kushiroite was also confirmed in the Allende and Murray carbonaceous chondrites [10], where the pyroxene contains the highest CaTs component yet reported among natural pyroxenes. Although the CaTs component is stable under high-pressure conditions [11], it also crystallizes metastably in low-pressure conditions from the refractory melt of solar nebula [12].

Here, we report on rare Al-rich pyroxenes from skarnoid xenoliths included in basaltic lava flow near Belina Hill in the northern part of the Pannonian Basin. We provide detailed mineralogical description of the associated paragenesis with the aim of reconstructing the thermal history and origin of the rocks described for the first time in the Carpathian realm.

2. Geological Setting

The Southern Slovakian Basin, consisting of the Lučenec Basin and the Cerova Highlands, is the northernmost promontory of the Pannonian Basin—an intra-Carpathian back-arc basin formed on a thinned crust in an extensional regime after Miocene subduction [13]. The alkali basalt volcanism in this area represents a typical intraplate association originated by the decompression melting of the upper mantle triggered by the diapiric updoming of the asthenospheric mantle [14–16]. The volcanic field, comprising maars, diatremes, necks, tuff cones, cinder/spatter cones and lava flows (Figure 1) resting upon Early Miocene sediments [17], extends over the area of 500 km^2 in Southern Slovakia and Northern Hungary. Volcanic rocks include basanites, alkali basalts and their derivatives—nepheline tephrite, trachybasalt and trachyandesite. Basaltic lava flows and pyroclastic deposits in maars contain fragments of igneous mafic cumulates, syenites and A1-type granitoids, which are unknown from the core mountains exposed in the Western Carpathians [18–22].

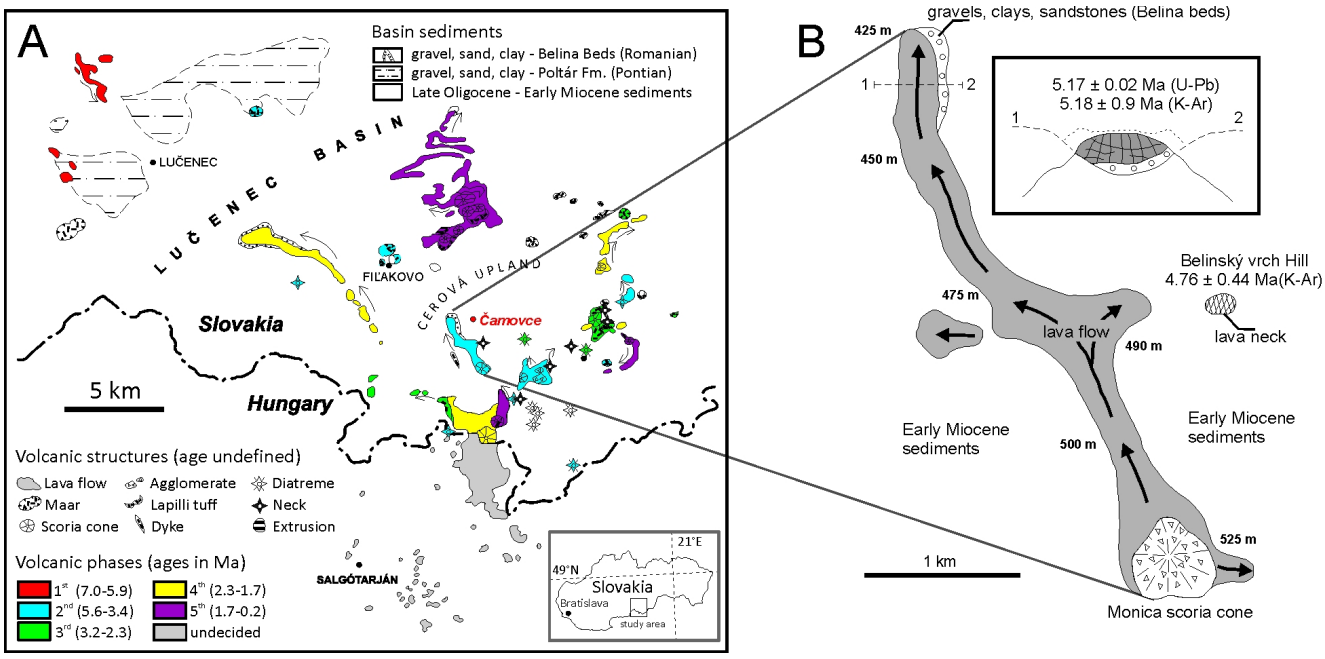

Figure 1. (**A**) Schematic map of the Southern Slovakia volcanic field, modified after [23]; (**B**) Enlarged view of the Belinsky vrch lava flow, lava neck and the Monica scoria cone. The 1–2 section transects the basalt quarry, where the xenoliths studied have been collected. Explanations: (**1**)—cinder cone, (**2**)—lava flow, (**3**)—gravels and clays of Belina beds, (**4**)—lava neck.

Sharp-edged calc-silicate xenoliths ranging in size from a few to 15 cm were collected in a quarry in the frontal part of the basanite lava flow of the Belina Hill located south of the Čamovce village (48°14′9.99″ N, 19°51′43.18″ E) in the Cerova Highlands (Figure 1). The lava flow has a K-Ar radiometric age of 5.17 ± 0.9 Ma [24], which is consistent with a 5.18 ± 0.02 Ma U-Pb age of zircon from granite xenoliths [19]. The NW-oriented lava flow erupted from the Monica volcanic center, recently scoria cone, located ~4 km SE and followed ancient valley. Its recent position on a ridge at the altitude of 425 m a.s.l. is due to a relief inversion caused by the uplift and extensive denudation of surrounding Early Miocene sediments [23]. Gravels and sandstones of Belina beds occur at the base of the lava flow. Presumable Late Pliocene (Romanian) age of the sediments is in conflict with the Early Pliocene (Dacian) age of the superimposed lava flow.

The Čamovce basalt exhibits porphyric texture with larger olivine and diopside phenocryst, up to 1 cm in size, in finely-grained groundmass composed of olivine, diopside, labradorite and rare nepheline and sodalite. From the geochemical point of view, the Čamovce lava flow is a fractionation product of basalt to nepheline-normative trachybasalt (hawaiite), showing the normalized distribution of trace elements typical of intra-plate alkali basalts. Granite fragments with A1-type geochemical signature [19] and mafic gabbroic cumulate xenoliths composed of diopside, olivine and Ca-plagioclase also occur in the Čamovce basalt recently exploited as macadam for local highway.

3. Materials and Methods

A total of eight xenoliths were studied. The samples have been described macroscopically to define structures, signs of interaction with basalt host and the presence of secondary alteration and/or weathering. After this, thin sections were prepared and inspected under transmitted light microscope to provide a general petrographic description and identification of the areas or mineral grains suitable for electron probe micro-analyses (EPMA), back-scattered electron imaging (BSE) and energy-dispersive X-ray mapping (EDSM).

Internal textures in 3D space have been visualized using an industrial micro-computer tomograph (micro-CT) v | tome | x L 240 maintained at the Institute of Earth Sciences SAS

in Banská Bystrica. The non-destructive X-ray tomograph with micro-focusing system and protective cabinet enables the rotation of object between fixed 240 kV X-ray tube and large-scale GE DXR detector with energy >12.4 keV. The X-ray tube provides the spatial resolution of up to μm-scale. Data processing was performed using the HP Z820 workstation equipped with two eight-core processors and the VGStudio MAX 2.2 software.

EPMA, BSE and EDSM studies were carried out using a CAMECA SX-100 electron microprobe (State Geological Institute D. Štúr, Bratislava, Slovakia), with the following analytical conditions: acceleration voltage of 15 kV, beam current of 20 nA and electron beam focused to 3–5 μm. Crystals, spectral lines and standards used were as follows: Si (TAP, Kα, wollastonite), Al (TAP, Kα, Al_2O_3), Ca (LPET, Kα, wollastonite), Fe (LLIF, Kα, fayalite), Ti (LPET, Kα, TiO_2), K (LPET, Kα, orthoclase), Na (TAP, Kα, albite), Mg (TAP, Kα, forsterite), Mn (LLIF, Kα, rhodonite), Cr (LLIF, Kα, Cr), Ni (LLIF, Kα, Ni), V (LLIF, Kα, V), Zn (LLIF, Kα, willemite). In addition, Sr (LPET, Lα, $SrTiO_3$) and S (LPET, Kα, barite) were measured in carbonates. Matrix effects were resolved using the X-PHI correction method [24]. If possible, spectral lines unaffected by interferences were selected. V-Ti, Cr-V and Mn-Cr interferences were corrected using empirical correction factors [25–27].

The ImageJ software [28] was used for noise reduction of EDSM compositional maps. Qualitative and quantitative filters have been applied to exclude erratic EPMA analyses. In the first step, the xenolith interactions with host basalt were verified under microscope. EPMA analyses from one sample were excluded from the dataset owing to extensive modification. The next step involved the raw EPMA data filtering. The interval between 98.5 and 101.5 wt% of oxides was accepted as threshold values for olivines. This filtering was not applied to ilmenite with depressed analytical totals due to the presence of ferric iron. After this, EPMA analyses were filtered according to their cation number [29]. Analyses with more than ±0.04 apfu deviation from the ideal formula based on 4 oxygen atoms for olivine and 3 oxygen atoms for ilmenite were excluded. This filtering was effective in the reduction of the data scattering.

A confocal Xplora Raman spectrometer from Horiba Ltd. (Kyoto, Japan) was used for spectroscopic characterization of carbonates. The system includes a flat-field 20 cm spectrograph with a multichannel air-cooled (−70 °C) Syncerity CCD detector and a color camera coupled to an Olympus BX-51 microscope. Raman spectra were collected with a 100× long-working-distance objective lens (NA = 0.8, WD = 3.4 mm) using a 532 nm excitation wavelength of a 25 mW solid-state Nd-YAG laser. A set of band-pass and edge filters collected the scattered light in the 50–4500 cm^{-1} region. Holographic grating with 1800 grooves/mm enabled maximal spectral resolution of 1.8 cm^{-1}/pixel. The spatial resolution corresponded to about 1 μm × 1 μm × 5 μm. Wavelength calibration was accomplished with a neon light source and the principal vibration band of silicon (520.7 cm^{-1}). Daily drift was corrected by regular measurements of the υ_1 vibration mode of atmospheric $^{14}N_2$ (2331 cm^{-1}).

4. Results

4.1. Petrography and Textures

Xenoliths studied are fragments, 5–20 cm in diameter, with sharp contacts against the basalt host (Figure 2). Larger xenoliths do not exhibit signs of interaction with the basalt host. Smaller xenoliths only show color alteration along the contact caused by the precipitation of Fe-oxy-hydroxides. Small fragments are sometimes detached from larger xenoliths and transposed in the surrounding basalt within the distance of the first hundred micrometers.

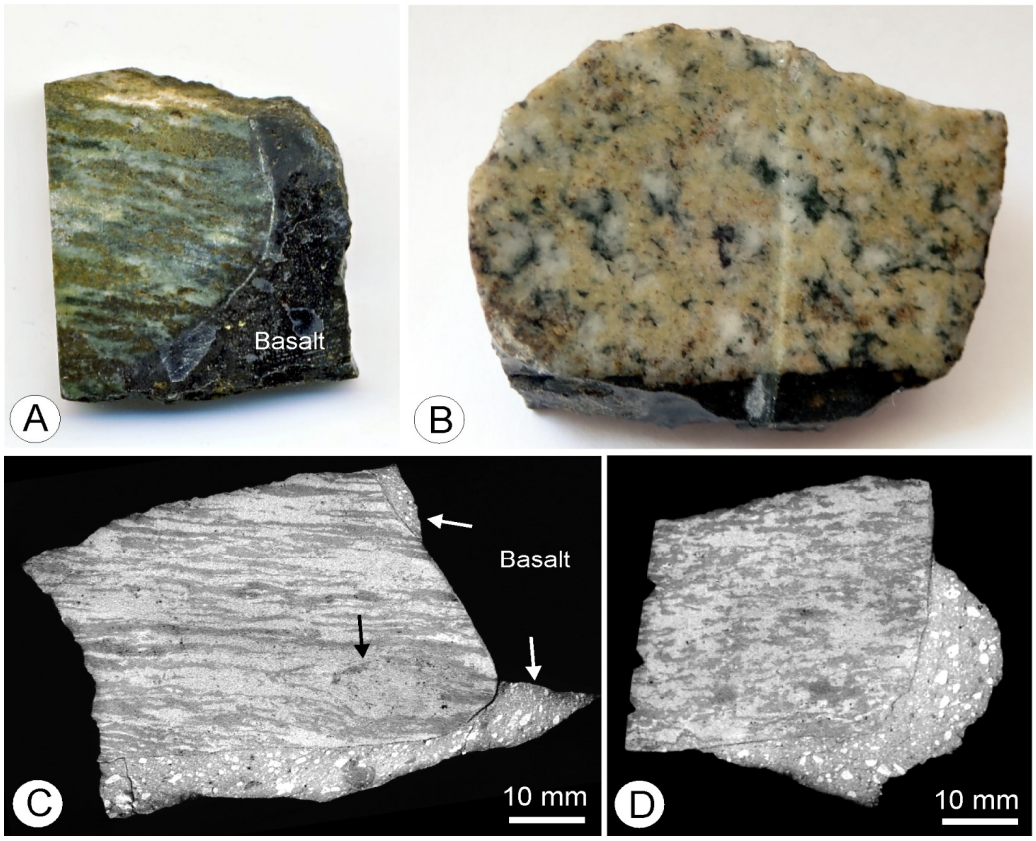

Figure 2. Skarnoid xenoliths in basalt from Čamovce quarry: (**A**) Banded texture of xenolith Ca-14, approximately 7 cm in size before cutting. Yellow-green bands are composed of olivine and pyroxene; (**B**) Granular texture in the section perpendicular to layering (sample Cam-13). Yellow parts correspond to olivine, dark green grains are pyroxenes and white areas are plagioclases. The xenolith is 5 cm in diameter; (**C**,**D**) Two differently oriented CT scans of xenolith Ca-14, showing banded, spindle-like texture in the longitudinal and speckled texture in the perpendicular section. Bright isolated grains in basalt correspond to olivine phenocrysts. Darker areas in xenoliths represent plagioclases, whereas brighter ones are mafic minerals, mainly pyroxene and olivine. Solid arrow in (**C**) designates the pod of mafic minerals.

In cm-scale, xenoliths exhibit banded gneissic texture with recurrent, compositionally contrasting, non-penetrative and anastomozing bright and darker layers. Two perpendicular CT cross-sections (Figure 2C,D) reveal dominant bright bands of mafic minerals with spindle-like shape intercalated by darker plagioclase-dominant layers.

The fabric revealed by CT scanning is in the first cross-section anisotropic, dominantly planar, with local ophtalmitic (podiform) structure (Figure 2C). The pale bands have elongated lenticular shapes. The rare symmetric lenticular pods are mafic mineral aggregates rather than true porphyroblasts. In general, the macroscopic texture displays features typical of mylonitic fabric. The elongated shape of layers defines the direction of stretching and tectonic transport. Asymmetric structures have not been detected, so the pure shear flattening was dominant in creating the observed texture. In perpendicular cross-section (Figure 2D), the mafic spindles become isometric, creating granular, more isotropic texture of the whole xenolith, with speckled appearance of interstitial plagioclase.

Ophitic texture observed in some xenoliths (Figure 3) is only discernible in thin sections as opaque laths composed of a finely-grained mixture of spinel and olivine randomly distributed in plagioclase groundmass. We are aware of the fact that the term ophitic texture is commonly used to describe plagioclase laths in mafic minerals, which is the situation reversal to that observed in xenoliths studied.

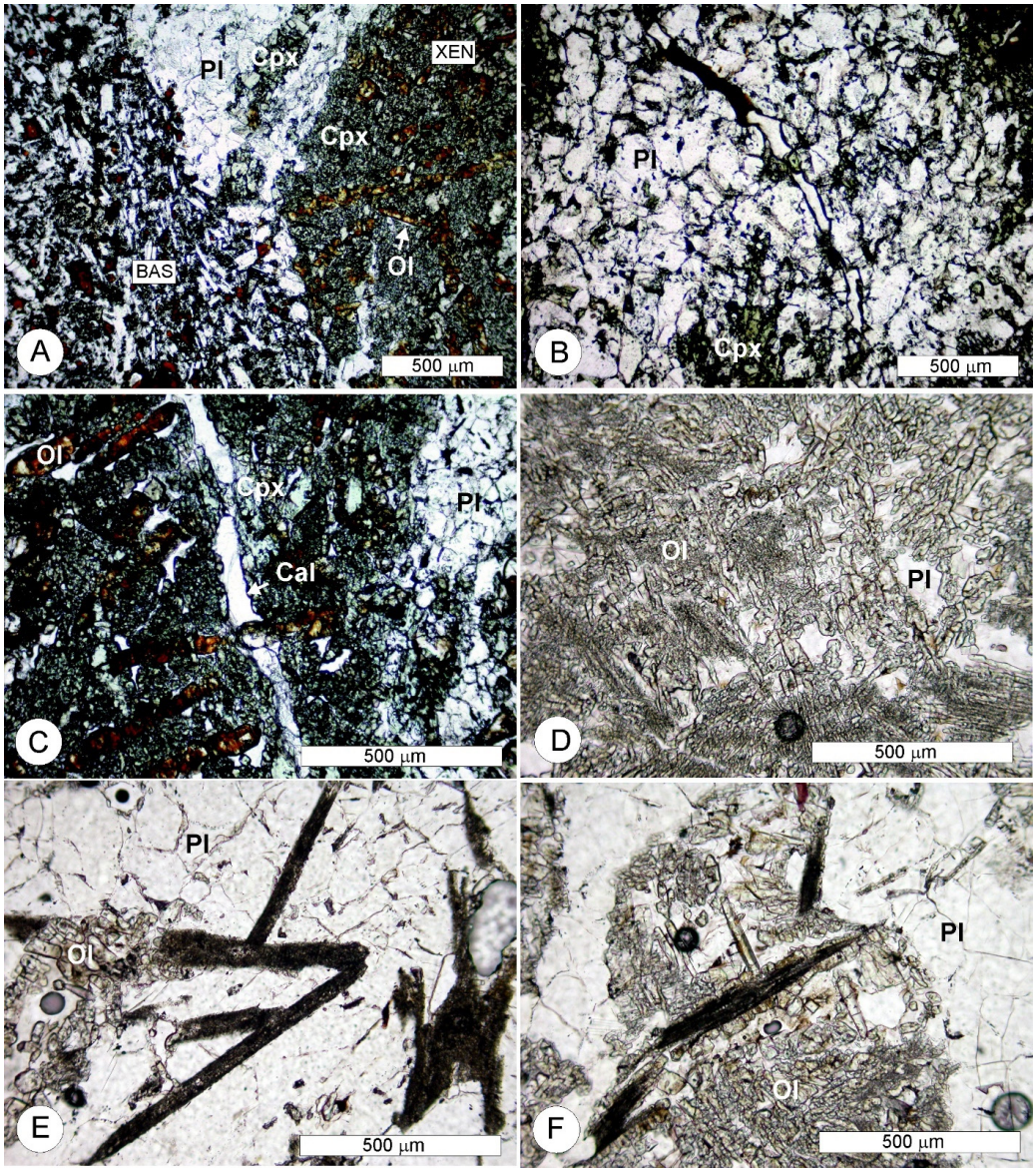

Figure 3. Photomicrographs of xenoliths in transmitted light: (**A**) Xenolith-basalt interface. Sample Ca-14. BAS and XEN denote basalt and xenolith, respectively; (**B**) Plagioclase layer with disseminated clinopyroxene grains and clusters. Sample Ca-14; (**C**) Pyroxene-rich layer with columnar olivine crystals growing across finely-grained pyroxene and carbonate. Sample Ca-14; (**D**) Columnar olivine chaotically distributed in plagioclase groundmass. Sample Ca-22; (**E**) Opaque, randomly oriented pseudomorphs composed of spinel, olivine and plagioclase in coarse-grained plagioclase layer. Sample Ca-22; (**F**) Pseudomorph epitaxially overgrown by columnar olivine crystals. Sample Ca-22. Mineral abbreviations in all photomicrographs after [29]: Ap—apatite, Cpx—clinopyroxene, Ol—olivine, Pl—plagioclase, Cal—calcite.

Microscopic observations revealed that the flattened, plan-parallel mafic spindles extending across whole xenoliths are composed of clinopyroxene aggregates and randomly oriented, elongated olivine crystals (Figure 3A–C). The plagioclase-rich parts are dominated by coarse-grained plagioclase with isolated clusters of clinopyroxene and spinel. Carbonates are also locally abundant. The columnar olivine occurs dominantly in mafic layers, but it also occurs in plagioclase layers in some xenoliths (Figure 3D).

The columnar olivine crystals and aggregates in mafic spindles reach lengths of several millimeters and grow over clinopyroxene I and pseudomorphs composed of olivine, clinopyroxene II and spinel II (Figure 3E). Terminal parts of the elongated olivine aggregates

are euhedral when protruding into carbonate pockets. Isolated, partly rounded olivine crystals also occur embedded in the carbonate groundmass. Olivine crystals are often altered to Fe-oxyhydroxides along margins and cracks.

Randomly oriented laths of fine-grained olivine-spinel-plagioclase aggregates cross-cut both mafic and plagioclase-rich layers (Figure 3E,F). The pseudomorphs have sharp contact against the surrounding minerals. The olivine-spinel-plagioclase paragenesis metasomatically replaces early spinel and plagioclase, thus creating an intersertal texture (Figure 4A–C).

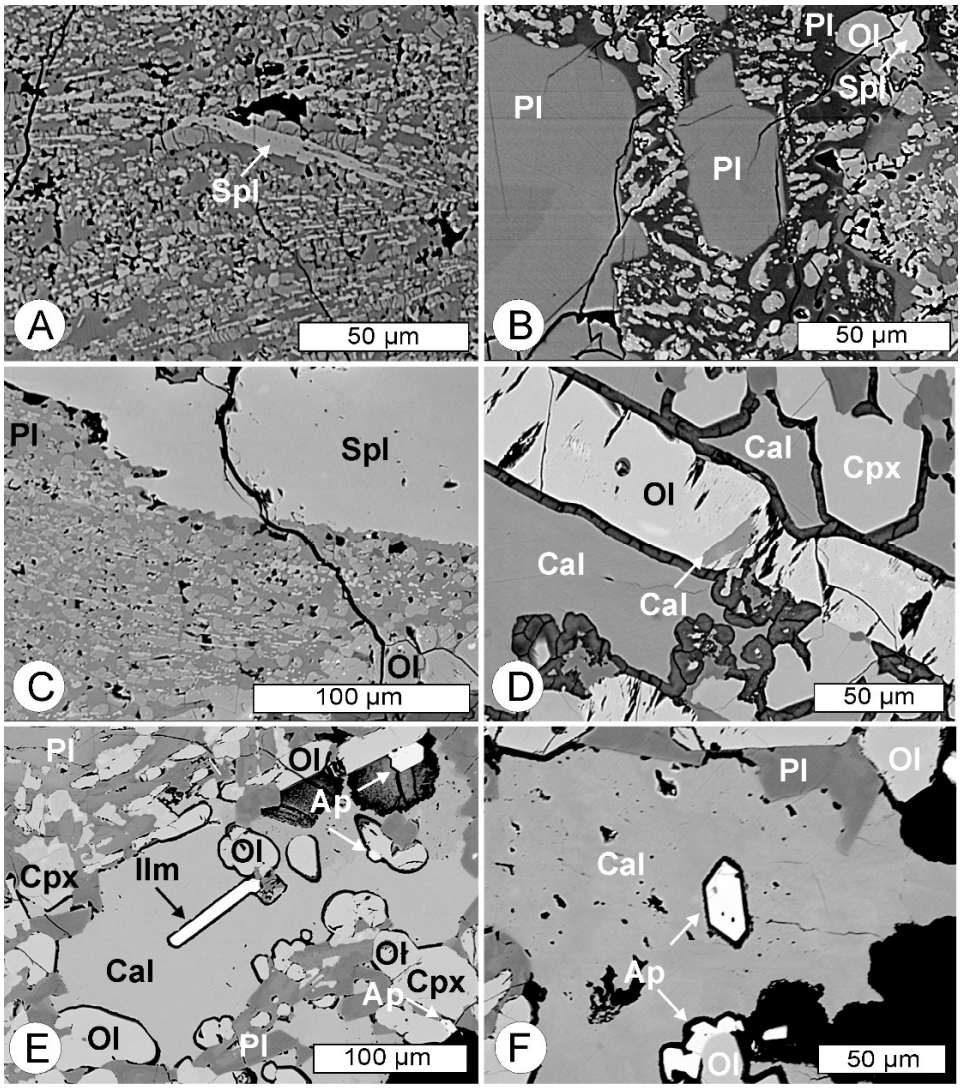

Figure 4. BSE images of rock-forming and superimposed minerals: (**A**) Enlarged view of pseudomorph with elongated spinel aggregates (bright) and isometric olivine crystals (medium bright) embedded in dark plagioclase groundmass. Sample Ca-45; (**B**) Replacement of early basic plagioclase with olivine, spinel and acidic plagioclase. Sample Ca-45; (**C**) Replacement of early spinel with olivine, spinel and acidic plagioclase. Sample Ca-45; (**D**) Columnar olivine II associated with carbonate growing across mafic layer composed of clinopyroxene I. Sample Cam-13; (**E**) Euhedral ilmenite growing from olivine substrate into carbonate groundmass. Sample Cam-13; (**F**) Euhedral apatite in carbonate growing over neoformed olivine II. Sample Cam-13. Mineral abbreviations in all photomicrographs after [30]: Cpx—clinopyroxene, Ol—olivine, Pl—plagioclase, Cal—calcite, Ilm—ilmenite, Ap—apatite, Spl—spinel.

4.2. Mineral Assemblages

The polyphase evolution of xenoliths is reflected in specific textures and mineral parageneses. Plagioclase and clinopyroxene are major rock-forming minerals accompanied by rare sulfides (chalcopyrite, pyrrhotite) postdated by spinel. Lath-shaped pseudomorphs are composed of spinel and olivine embedded in plagioclase groundmass (Figure 4A). An amphibole grain, 10 μm in size, was detected in one pseudomorph.

The olivine-spinel-plagioclase paragenesis identical to that in pseudomorphs also metasomatically replaces rock-forming plagioclase I and spinel I (Figure 4B,C). Spinel crystals in pseudomorphs often show preferred direction of growth of parallel-oriented, elongated crystals grouped in fan-like aggregates (Figure 4A,C). In contrast, coexisting olivine crystals are isometric and tend to increase their dimensions from several μm in centers to several tens of μm along pseudomorph margins epitaxially overgrown by larger columnar olivine II (Figure 3F), which crosscuts mafic spindles and grows at the expense of clinopyroxene I (Figure 4D). The olivine II is often associated with carbonates, plagioclase II, ilmenite and apatite (Figure 4D–F).

The mineral paragenesis attributed to thermal overprint by surrounding basalt has been recognized only in some xenoliths as amoeboid corundum exsolutions from plagioclase and intergranular infillings of plagioclase, K-feldspar, biotite, sodalite, nepheline, magnetite, ilmenite II and apatite II. Succession scheme based on observations of thin sections under polarized microscope and BSE (Figure 5) makes the subdivision among pseudomorph, carbonate and alkali metasomatic parageneses, although they may represent various stages of the same process taking place in different depths and temperatures.

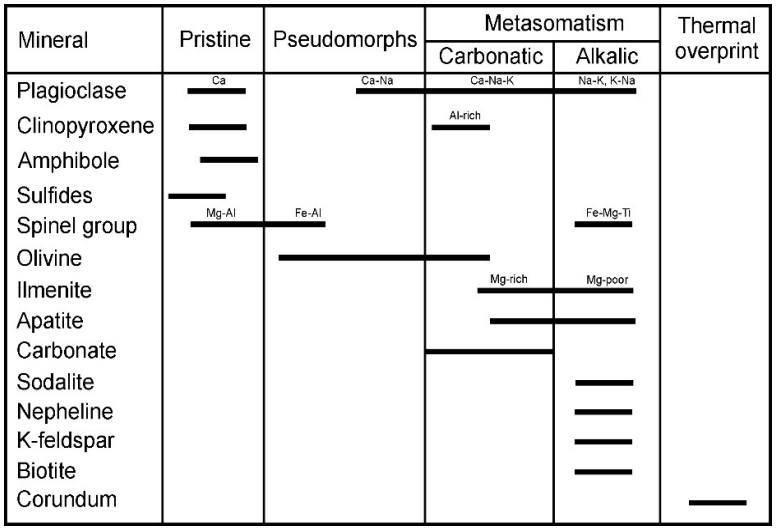

Figure 5. Succession of crystallization and mineral parageneses in calc-silicate xenoliths from Čamovce.

4.3. Mineral Compositions

4.3.1. Plagioclase

Plagioclase-rich layers are composed of $An_{93–100}$ anorthite, whereas plagioclases in mafic spindles vary from anorthite cores to bytownite ($An_{89–85}$) rims in contact with olivine aggregates. $Ab_{58–64}$ plagioclase occurs in the proximity of carbonate pockets and clusters in mafic spindles, and similar composition ($An_{57–86}$) was recorded in plagioclase inclusions in olivine and diopside-augite. Interstitial plagioclases vary from An_{67} andesine to An_{37} oligoclase. Plagioclases in pseudomorphs fluctuate from An_{96} anorthite to An_{53} labradorite (Figure 6). Albite crystallizes as a member of the interstitial alkali metasomatic paragenesis together with Or_{63} sanidine, biotite, ilmenite, magnetite and sodalite.

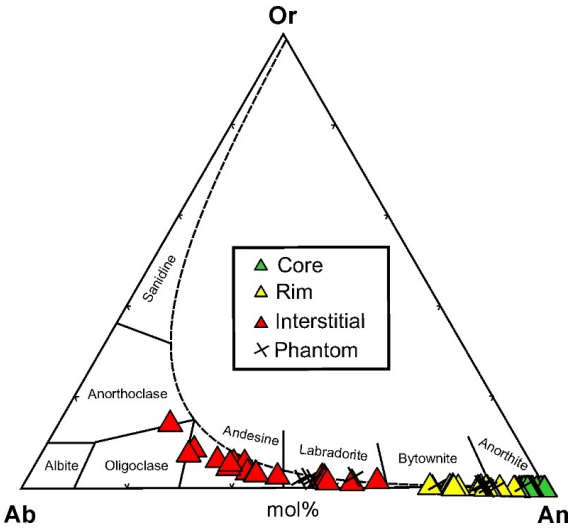

Figure 6. Ternary Ab-An-Or classification diagram of plagioclases with miscibility gap (dashed curve) calculated for 900 °C and 1 GPa using the ternary feldspar mixing model [31].

Significant iron enrichment in Fe has been observed in all plagioclase types. The gradual Fe enrichment accompanied by the increasing plagioclase acidity (correlation coefficient $r^2 = 0.7$) reflects the coupled Fe^{3+} for Al^{3+} and Na+K for Ca substitution (Supplementary Table S1). This trend is valid for anorthite contents below 80 mol%. More basic plagioclases show unsystematic distribution of Fe contents, although the total range of Fe_2O_3, 0.07–1.03 wt%, is somewhat wider than that in more acidic plagioclases (0.18–0.92 wt%).

4.3.2. Pyroxene

Pyroxenes in mafic spindles correspond to the diopside-augite series. In contrast, pyroxenes from plagioclase-rich layers cover the range from common Ca-Mg-Fe clinopyroxenes of diopside-augite series, plotting within the QUAD field in the *J*–*Q* diagram, to other pyroxenes with $J + Q < 1.5$ (Figure 7A,B). The QUAD pyroxenes projecting in diopside and augite fields in the Wo-En-Fs classification diagram can be classified as ferroan-to-ferrian, aluminian diopside and aluminian augite. Some QUAD pyroxenes with higher Al and Fe^{3+} contents plot within the wollastonite field, despite the subtracting Ca-Tschermak components before the classification.

The $J + Q < 1.5$ group projects in kushiroite ($CaAl[AlSiO_6]$) and esseneite ($CaFe^{3+}[AlSiO_6]$) fields in the QUAD-Ess-Ks diagram (Figure 7C,D), creating a continuous mixing trend from the QUAD diopside to a component with approximately equal proportion of kushiroite and esseneite molecules. The mixing trend (Figure 7E) is directly related to the coupled substitution: $Si^{4+} + Mg^{2+} = Fe^{3+} + Al^{3+}$ described in [2,7]. Si and Al^{3+} are the only cations in the tetrahedral site, as the content of Fe^{3+} and the Fe^{3+}/Al^{3+} ratio are not high enough to allow for the tetrahedrally coordinated $^{IV}Fe^{3+}$.

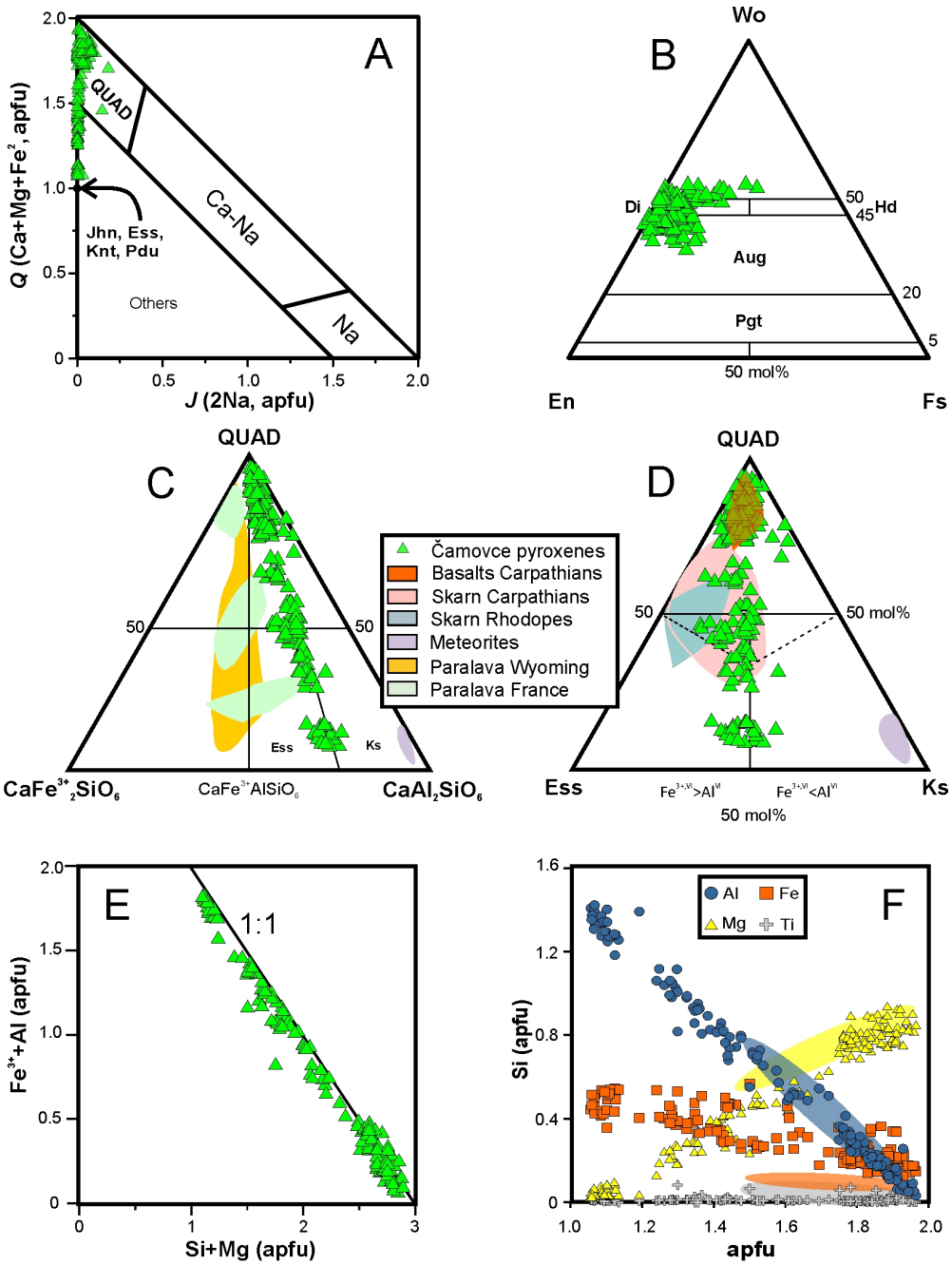

Figure 7. Classification diagrams and compositional trends of pyroxenes: (**A**) *J*–*Q* classification diagram for pyroxenes [32] with projection of pyroxenes from Čamovce; (**B**) Classification diagram of QUAD pyroxenes; (**C**,**D**) Classification diagrams for pyroxenes from the Čamovce with fields for pyroxenes from carbonaceous chondrites [10–12], paralavas of the Lapanouse-de-Sévérac region, France [3] and WY, USA [2]; skarns of the Romanian Carpathians [7] and Rhodopes, Bulgaria [33]. The orange, semitransparent area in D denotes the field of magmatic Al-rich clinopyroxenes from south Slovakian basalts formed by the interaction with carbonate-syenite xenoliths (unpublished); (**E**) Coupled substitution Fe^{3+} + Al = Si+Mg in pyroxenes from Čamovce; (**F**) Relations among Al, Fe (total), Mg, Ti and Si for pyroxenes from Čamovce. Colored ellipses express the compositional range of pyroxenes from skarns in Romanian Carpathians [7]. Wo contents in (**B**–**D**) have been calculated from the residual Ca (apfu) after creating Ca-Tschermak components ($CaTiAl_2O_6$, $CaFe^{3+}{}_2SiO_6$ and $CaAl_2SiO_6$). Mineral abbreviations [30]: Jhn—johannsenite, Ess—esseneite, Ks—kushiroite, Di—diopside, Hd—hedenbergite, Wo—wollastonite, En—enstatite, Fs—ferrosilite, Aug—augite, Pgt—pigeonite, Knt—kanoite, Pdu—petedunnite.

The Al,Fe^{3+}-rich pyroxenes from Čamovce show variable zoning patterns depending on grain dimensions (Figure 8). Smaller grains are only moderately zoned and usually have Al,Fe-rich compositions across the whole grain, or esseneite core surrounded by diopside rim. Bigger grains usually exhibit an irregular domain pattern with diopside core and esseneite-kushiroite rims, in which esseneite-rich parts occur along contacts with carbonate, and the kushiroite component prevails in zones adjacent to anorthite (Figure 8A–C).

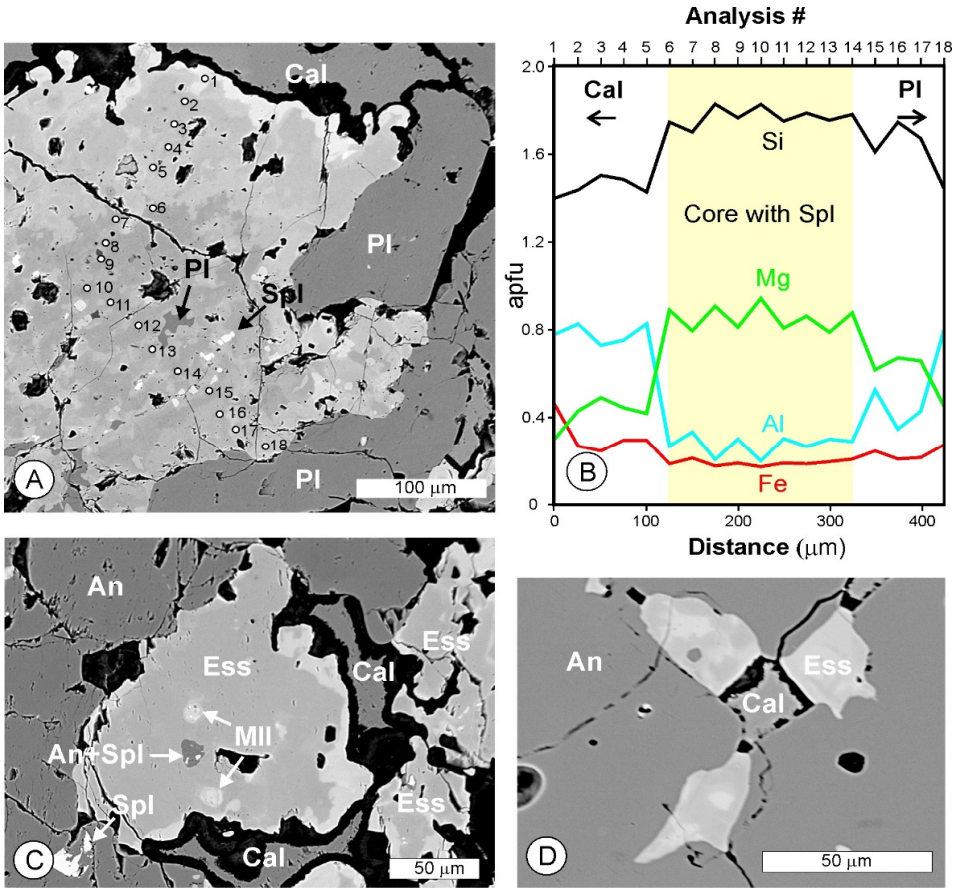

Figure 8. (**A**) Zoned Al,Fe^{3+} pyroxene in contact with calcite and anorthite, showing esseneite margins and diopside core with abundant spinel inclusions. The measured EPMA profile (**B**) and the irregular domain zoning is reminiscent of a diffusion pattern. Note also the Fe-rich zone at the contact with calcite missing along the pyroxene-anorthite interface; (**C**) Melilite and anorthite+spinel inclusions in esseneite grain attached to calcite in anorthite layer. Esseneite has Fe^{3+}-enriched margins along the contact with carbonate; (**D**) Inverse zonation pattern with bright esseneite cores surrounded by more diopsidic rims. All photomicrographs refer to sample Ca-14. Mineral abbreviations [30]: Mll—melilite, Spl—spinel, An—anorthite, Ess—esseneite, Cal—calcite, Pl—plagioclase.

Elemental X-ray distribution maps of pyroxenes enhance the combination of dominant domain and subordinate growth zoning (Figure 9), with almost constant Ca contents regardless of the pyroxene composition. Documented also is the antagonistic behavior of Si against Al, and positively correlated Al, Fe and Cr and their negative correlation with Mg. Worth noting is rather uniform Ti distribution regardless of Fe and Al contents in whole grain, except for local domains in edges substantially enriched in Ti (up to 2.8 wt% TiO_2) and Fe, and depleted in Al. The Ti,Fe-rich edges create compositionally contrasting esseneite subgroup characterized by increased vanadium concentrations, up to 2.1 wt% V_2O_3 (Table 1, analysis #15).

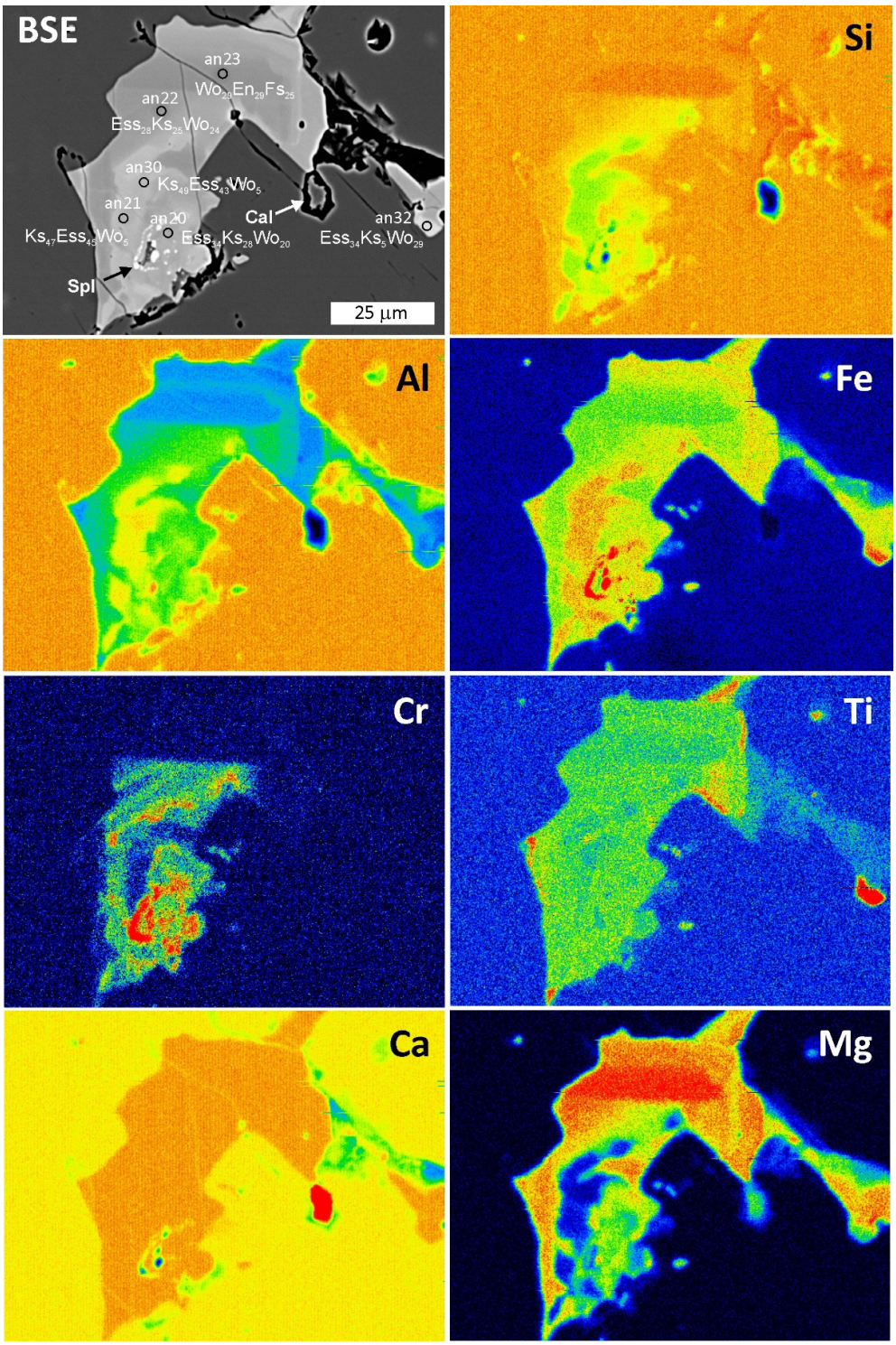

Figure 9. BSE image and false color-coded X-ray maps of esseneite-diopside grain in sample Cam-14. Note locally increased Ti (and V) contents along grain boundaries enriched in Fe and depleted in Al (analysis #32, Table 1). Spinel inclusions are diagnostic of the highest Cr and Fe concentrations. Warmer colors (red, orange) denote higher concentrations.

Table 1. Representative EPMA analyses, crystal chemistry and endmembers of clinopyroxenes.

Sample	Cam-14								Ca-14				Ca-14 ◊		
Analysis #	**15**	**20**	**22**	**23**	**21**	**30**	**32**	**69**	**11**	**52**	**64**	**90**	**1**	**10**	**18**
SiO_2 (wt%)	32.95	35.06	37.76	44.03	27.44	27.77	38.20	28.02	27.55	36.06	33.07	28.79	36.54	50.49	38.78
TiO_2	2.76	0.47	0.39	0.32	0.36	0.22	2.21	0.21	0.30	0.28	0.36	b.d.l.	0.65	0.12	0.31
Al_2O_3	17.60	20.64	18.42	11.83	31.01	31.41	11.94	27.35	31.12	21.48	21.47	27.06	17.28	4.66	18.83
Fe_2O_3 *	14.58	11.44	9.49	8.95	15.31	14.75	10.49	16.04	14.41	10.89	13.73	15.41	12.55	4.78	10.37
Cr_2O_3	b.d.l.	0.99	1.14	b.d.l.	0.63	0.22	b.d.l.	0.19	0.32	0.23	0.71	0.19	0.18	0.06	0.02
V_2O_3	2.09	0.02	0.01	0.09	b.d.l.	b.d.l.	1.28	n.a.	n.a.	n.a.	n.a.	n.a.	n.a.	n.a.	n.a.
FeO	2.98	1.62	0.53	0.38	0.05	0.00	7.98	1.31	1.14	0.71	1.28	2.51	2.92	1.41	0.00
NiO	b.d.l.	b.d.l.	b.d.l.	b.d.l.	0.02	0.03	b.d.l.	0.01	0.01	b.d.l.	0.02	0.02	0.01	b.d.l.	0.01
MnO	0.27	0.05	0.01	0.10	0.03	b.d.l.	0.53	0.06	0.01	0.04	0.05	0.09	0.18	0.18	0.05
MgO	3.19	5.15	7.43	10.60	0.85	0.78	4.03	0.58	0.55	6.13	3.90	0.61	5.32	17.48	8.03
CaO	23.74	24.46	24.75	24.95	24.60	24.97	24.16	24.89	24.63	24.95	24.97	24.38	24.48	20.96	25.37
K_2O	b.d.l.	0.01	b.d.l.	b.d.l.	b.d.l.	b.d.l.	b.d.l.	b.d.l.	b.d.l.	b.d.l.	b.d.l.	b.d.l.	b.d.l.	0.01	b.d.l.
Na_2O	0.11	0.03	b.d.l.	0.32	b.d.l.	b.d.l.	0.08	b.d.l.	b.d.l.	b.d.l.	b.d.l.	b.d.l.	0.06	0.18	0.02
Total	100.28	99.94	99.94	101.58	100.29	100.15	100.89	98.69	100.04	100.78	99.57	99.06	100.18	100.32	101.79
Si (apfu)	1.298	1.342	1.427	1.622	1.056	1.066	1.498	1.108	1.064	1.356	1.283	1.135	1.407	1.837	1.433
Al^{IV}	0.702	0.658	0.573	0.378	0.944	0.934	0.502	0.892	0.938	0.646	0.718	0.866	0.593	0.163	0.567
Al^{VI}	0.115	0.274	0.247	0.136	0.462	0.488	0.050	0.383	0.477	0.304	0.263	0.391	0.191	0.037	0.253
Ti	0.082	0.013	0.011	0.009	0.011	0.006	0.065	0.006	0.009	0.008	0.010	0.000	0.019	0.003	0.009
Fe^{3+}	0.432	0.330	0.270	0.248	0.443	0.426	0.328	0.477	0.419	0.308	0.401	0.457	0.364	0.131	0.288
Cr	0.000	0.030	0.034	0.000	0.019	0.007	0.000	0.006	0.010	0.007	0.022	0.006	0.005	0.002	0.001
V	0.066	0.001	0.000	0.003			0.040								
Fe^{2+}	0.098	0.052	0.017	0.012	0.002	0.000	0.244	0.043	0.037	0.022	0.042	0.083	0.094	0.043	0.000
Ni					0.001	0.001					0.001	0.001	0.000		
Mn	0.009	0.002	0.000	0.003	0.001	0.000	0.018	0.002		0.001			0.006	0.006	0.002
Mg	0.187	0.294	0.418	0.582	0.049	0.045	0.235	0.034	0.032	0.343	0.226	0.036	0.305	0.948	0.442
Ca_{M1}	0.076	0.005	0.002	0.008	0.014	0.027	0.021	0.054	0.019	0.005	0.038	0.029	0.015	0.000	0.006
Ca_{M2}	0.926	0.998	1.000	0.977	1.000	1.000	0.994	1.000	1.000	1.000	1.000	1.000	0.995	0.817	0.998
K	0.000	0.000												0.000	
Na	0.008	0.002	0.000	0.023	0.000	0.000	0.000						0.005	0.013	0.002
Total	3.999	4.001	3.999	4.001	4.002	4.000	3.995	4.007	4.005	4.003	4.005	4.006	3.999	4.000	4.001
Q	1.29	1.35	1.44	1.58	1.06	1.07	1.49	1.13	1.09	1.37	1.31	1.15	1.41	1.81	1.45
J	0.02	0.00	0.00	0.05	0.00	0.00	0.01	0.00	0.00	0.00	0.00	0.00	0.01	0.03	0.0
Jd	0.9	0.2	0.0	2.3	0.0	0.0	0.6	0.0	0.0	0.0	0.0	0.2	0.5	1.3	0.2
Ess	44.7	33.5	27.5	24.6	44.8	42.8	33.6	48.7	43.3	31.8	41.4	46.7	36.5	13.1	28.9
CaTi-Ts	8.4	1.4	1.1	0.9	1.1	0.6	6.7	0.6	0.9	0.8	1.0	0.0	1.9	0.3	0.9
Ks	11.9	27.8	25.2	13.4	46.6	49.0	5.1	38.1	47.5	33.0	26.4	38.8	19.2	3.7	25.3
Wo	19.3	19.6	24.1	29.4	5.0	5.4	29.4	8.7	4.9	17.3	17.7	8.3	21.9	32.2	22.7
En	9.7	14.9	21.3	28.9	2.5	2.2	12.1	1.7	1.6	17.1	11.3	1.8	15.3	47.3	22.1
Fs	5.1	2.6	0.9	0.6	0.1	0.0	12.5	2.2	1.9	0.0	2.2	4.2	4.7	2.1	0.0
QUAD	34.1	37.2	46.2	58.8	7.5	7.6	54.0	12.6	8.4	34.4	31.1	14.4	41.9	81.7	44.8
Name **	Ess	Ess	Ess	Wo	Ks	Ks	Ess	Ess	Ks	Ks	Ess	Ess	Ess	En	Ess

* Fe^{2+}/Fe^{3+} ratio calculated after [34]; ** Dominant constituent rule [35]; ◊ EPMA profile in Figure 8A,B; b.d.l.—below detection limit, n.a.—not analyzed; Abbreviations: Jd—jadeite, Ess—esseneite, CaTi-Ts—Ca,Ti-Tschermak component, Ks—kushiroite, Wo—wollastonite, En—enstatite, Fs—ferrosilite, QUAD—Wo+En+Fs, $Q = Fe^{2+}+Ca+Mg$, $J = 2Na$.

4.3.3. Olivine

Olivines from Čamovce xenoliths span the compositional range of $Fo_{66–88}$ (Supplementary Table S2). Almost ideal negative Fe-Mg ($r^2 = 0.99$) and strong positive Fe-Mn ($r^2 = 0.76$) correlations indicate dominant fayalite-forsterite and fayalite-tephroite solid solution trends. A weak positive correlation between Fe and Ca ($r^2 = 0.36$) indicates preferential incorporation of calcium in more fayalitic olivine.

Olivines in pseudomorphs are close to the upper limit of the overall compositional range ($Fo_{85}–Fo_{88}$), whereas columnar olivines associated with ilmenite in carbonate pockets are more fayalitic, creating the $Fo_{79}–Fo_{81}$ cluster with one outlier (Fo_{83}). Tephroite and Ca_2SiO_4 endmember contents are decreased in the pseudomorph olivines (0.25 and 0.39 mol% in average, respectively) compared to carbonate-hosted olivines (0.35 and 0.51 mol% in average, respectively).

Crystal structure of olivine enables small concentrations of Fe^{3+} to be incorporated in the octahedral site [36]. The possible occurrence of Fe^{3+} in olivines from Čamovce is indicated by the excess of cations in the formula recalculated to 4 oxygen atoms. The maximum Fe_2O_3 content back-calculated from the stoichiometry corresponds to 4.7 wt%. Pseudomorph olivines seem to be more oxidized (1.1–4.7 wt% Fe_2O_3, 2.9 wt% in average) compared to carbonate-hosted columnar olivines associated with ilmenite (0.3–2.3 wt% Fe_2O_3, 1.3 wt% in average).

4.3.4. Amphibole

An amphibole was detected in one pseudomorph as irregular grain embedded in the compositionally variable plagioclase (Figure 10). The Mg/Mg+Fe^{2+} ratio (0.86–0.93), low Si contents (6.14 and 6.20 apfu) and strong Al^{3+} predominance over Fe^{3} in the octahedral site is diagnostic of tschermakite (Table 2). Crystal chemical formula calculated from EPMA analyses corresponds to:

$$(\square_{0.90\text{-}0.91}Na_{0.07\text{-}0.09})(Ca_{1.58\text{-}1.61}Na_{0.36\text{-}0.39})(Mg_{2.46\text{-}2.66}Fe^{2+}{}_{0.21\text{-}0.42})(Al^{VI}{}_{1.95\text{-}2.10}Fe^{3+}{}_{0\text{-}0.19})$$
$$(Al^{IV}{}_{1.80\text{-}1.86}Si_{6.14\text{-}6.20})O_{22}(OH)_2$$

and projects close to the ideal tschermakite endmember $\square Ca_2(Mg_3Al_2)(Al_2Si_6O_{22}(OH)_2$ (Figure 11).

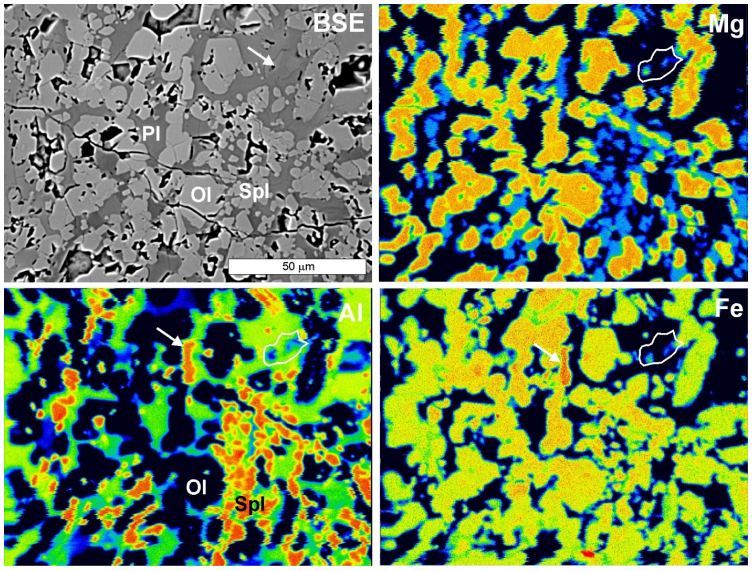

Figure 10. BSE image and false color-coded X-ray maps of pseudomorph with irregular amphibole grain (white arrow, contoured in X-ray maps) associated with olivine (Ol), Mg,Al-spinel (Spl) and plagioclase (Pl). Sample Cam-15. Note also hercynite grain indicated by white arrows in Al and Fe distribution maps. Warmer colors (red, orange) denote higher concentrations.

Table 2. Representative EPMA analyses and crystal chemistry of amphibole (sample Cam-15).

EPMA (wt% Oxide)			Formula Based on 24 (O, OH, F, Cl)			
Analysis	**9**	**14**			**9**	**14**
SiO_2	44.96	45.45	T (8 apfu)	Si	6.144	6.204
TiO_2	0.01	0.01		Al	1.856	1.796
Al_2O_3	23.62	24.21	C (5 apfu)	Ti	0.001	0.001
Cr_2O_3	b.d.l.	b.d.l.		Al	1.948	2.100
NiO	0.01	0.01		Fe^{3+}	0.187	
Fe_2O_3 *	1.82	0.00		Mn^{2+}		0.009
FeO	2.22	3.65		Fe^{2+}	0.208	0.417
MnO	0.07	0.08		Mg	2.656	2.464
MgO	13.04	12.11		C subtotal	5.000	4.991
CaO	10.78	11.01	B (2 apfu)	Mn^{2+}	0.008	
Na_2O	1.65	1.80		Fe^{2+}	0.046	
K_2O	0.10	0.10		Ca	1.579	1.611
Cl	b.d.l.	b.d.l.		Na	0.368	0.389
F	b.d.l.	b.d.l.	A (1 apfu)	Na	0.070	0.088
H_2O^+	1.69	1.69		K	0.017	0.017
Total	99.96	100.10		□	0.913	0.895
			W (2 apfu)	OH	2.000	2.000

b.d.l.—below detection limit; * calculated from stoichiometry [37].

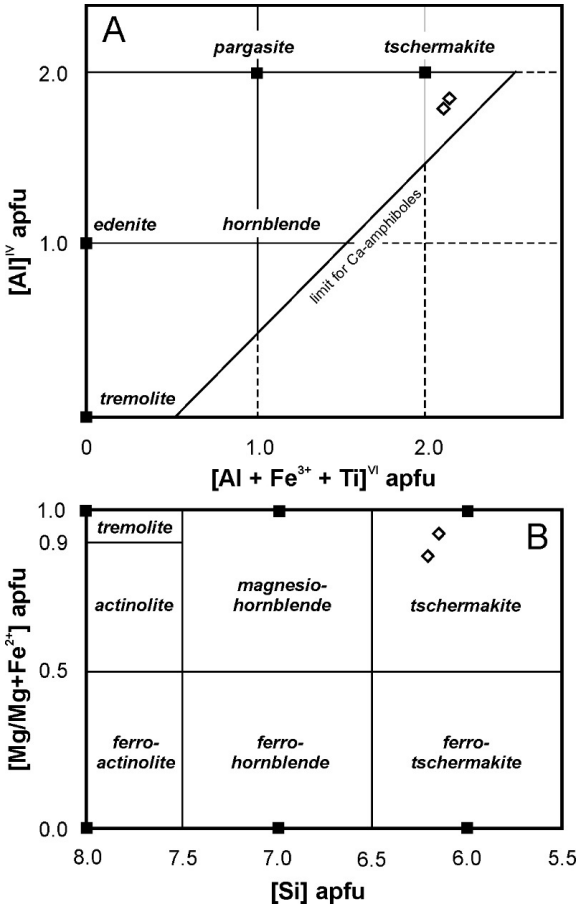

Figure 11. (**A**) Plot of Al^{IV} versus Al^{VI}+Fe^{3+}+Ti [38] for amphibole from Čamovce (open diamonds) with projections of ideal endmembers (solid squares); (**B**) Classification diagram of calcic amphiboles [39] with projections of data from Čamovce (open diamonds) and ideal endmembers (black squares).

4.3.5. Carbonates

Carbonates are present as clusters and pockets interconnected by thin veinlets. Volumetric proportions of carbonates change from one xenolith to the other. If present, the carbonates are much more abundant in mafic spindles compared to plagioclase-rich parts.

X-ray elemental distribution maps and cross-polarized transmitted light images (Figure 12) reveal isolated carbonate crystals and twins embedded in coarse-grained carbonate groundmass or growing from the outer perimeter of carbonate pockets. Raman spectroscopy confirmed aragonite crystals embedded in calcite or aragonite groundmass in three of eight investigated xenoliths. The aragonite is diagnostic of the band at 701 cm^{-1} and several typical vibrations in the low-frequency region compared to four bands at 153, 281, 713 and 1089 cm^{-1}, in well-crystallized calcite groundmass (Figure 13).

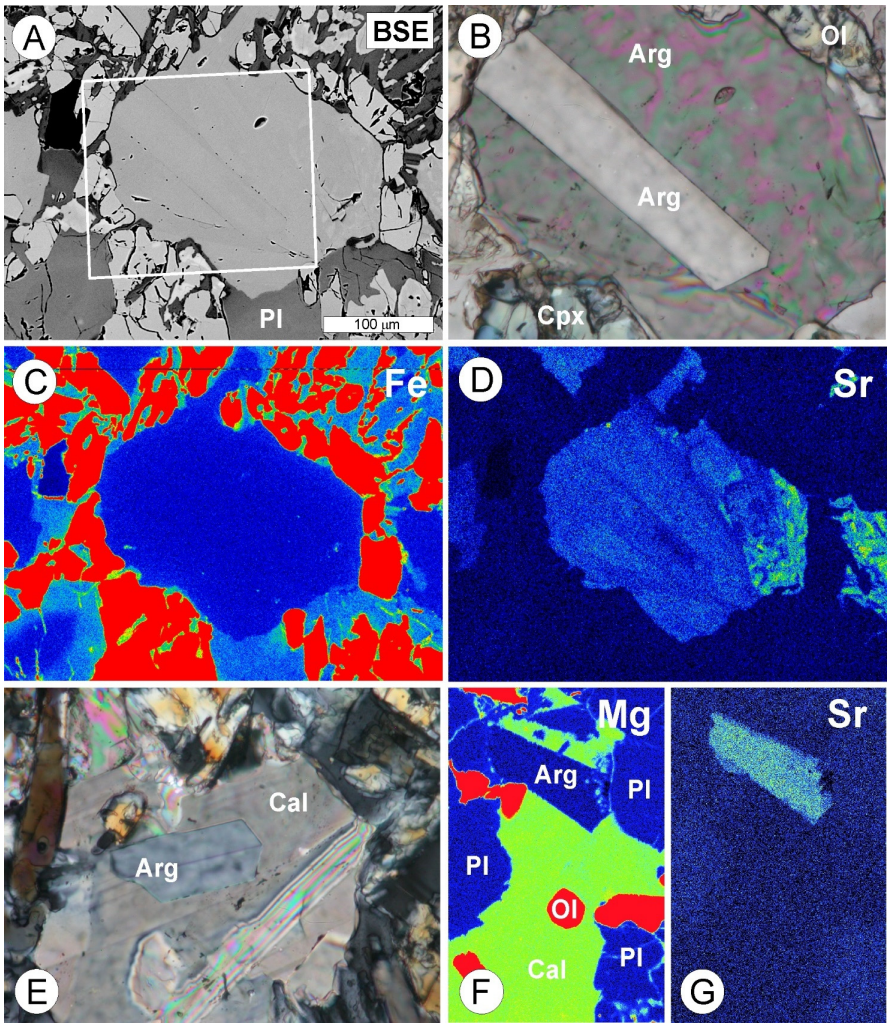

Figure 12. X-ray maps, transmitted light, and BSE images of carbonates in mafic layers in sample Cam-13: (**A**) BSE image of carbonate pocket showing blocky mosaic texture and one elongated crystal transversal to the square field; (**B**) Partly cross-polarized, transmitted light image of the square field in (**A**), showing euhedral aragonite in aragonite crystal aggregate with variegated interference colors; (**C**) False color-coded X-ray map of iron in (**A**), showing diffusion gradients of iron in plagioclase touching the carbonate pocket and olivine crystals growing at the expense of clinopyroxene in the carbonate; (**D**) False color-coded X-ray map of Sr distribution, showing increased Sr contents in aragonite crystal and local Sr-rich domains in the aragonite matrix; (**E**) Cross-polarized, transmitted light image of aragonite twin in calcite matrix; (**F**,**G**) False color-coded X-ray map of Mg and Sr distribution showing Sr-rich, Mg-poor aragonite crystal in Mg-rich, Sr-poor calcite groundmass. Warmer colors in (**C**,**D**,**F**,**G**) denote higher concentrations. Mineral abbreviations [30]: Arg—aragonite, Cal—calcite, Pl—plagioclase, Ol—olivine, Cpx—clinopyroxene.

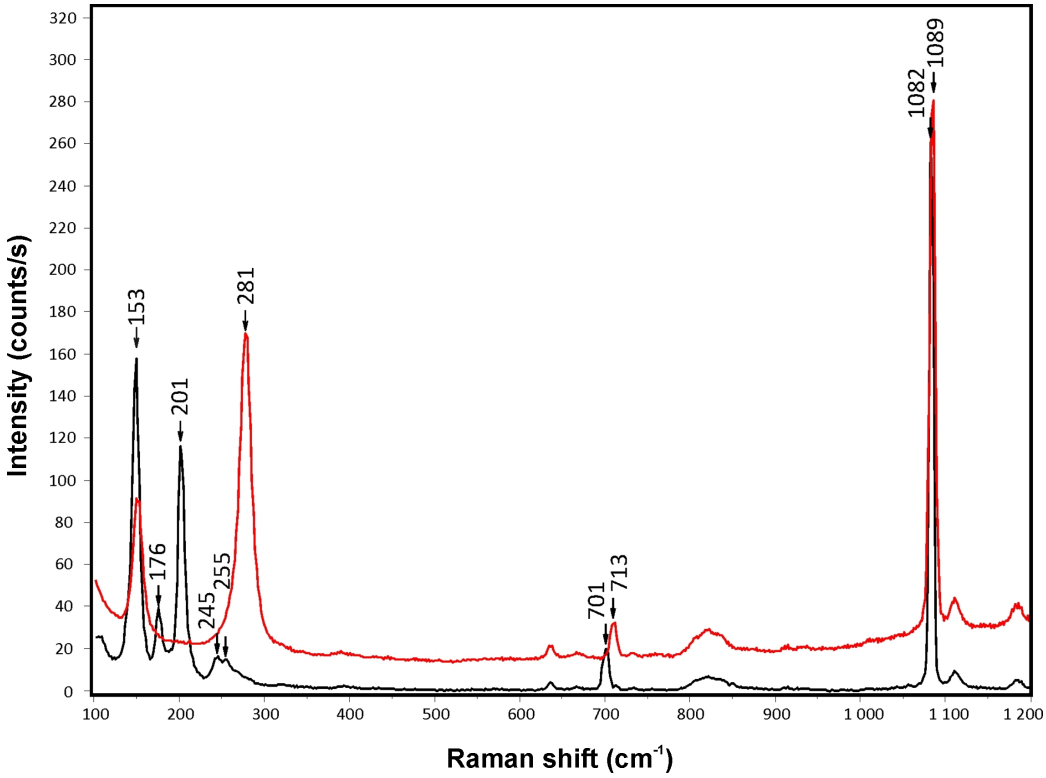

Figure 13. Uncorrected Raman spectra of aragonite crystal (black spectrum) and calcite groundmass (red spectrum) shown in Figure 12E. Spectra are offset for clarity. Not assigned bands are spectral artifacts from organic glue.

Carbonate veinlets cutting olivine and plagioclase layers, indistinctly, does not differ in terms of composition. EPMA revealed an ideal, negatively correlated linear substitution trend between $CaCO_3$ and $MgCO_3$ endmembers in calcite, with maximum MgO contents reaching 1–3 wt%. In contrast, none or negligible amounts of MgO have been detected in aragonite, which is typical of increased Sr concentrations, ranging between 0.5 and 3.2 wt% SrO.

4.3.6. Spinel-Group Minerals

Spinel-group minerals in Čamovce xenoliths occur as isolated grains and aggregates embedded in rock-forming anorthite (type 1), aggregates associated with olivine in pseudomorphs (type 2), inclusions in clinopyroxene I and olivine II (type 3) and grains associated with rhombohedral Fe,Ti-oxides in alkali metasomatic paragenesis (type 4).

Spinel-group minerals in Čamovce xenoliths comprise solid solution series among three dominant endmembers: spinel $MgAl_2O_4$ (max. 76 mol%), magnetite $FeFe_2O_4$ (max. 75.5 mol%) and hercynite $FeAl_2O_4$ (max. 46.5 mol%). Discrete ulvöspinel group with 82–90 mol% Fe_2TiO_4 occurs only in the xenolith Ca-21B as a member of the alkali metasomatic paragenesis (Figure 14, Supplementary Table S3).

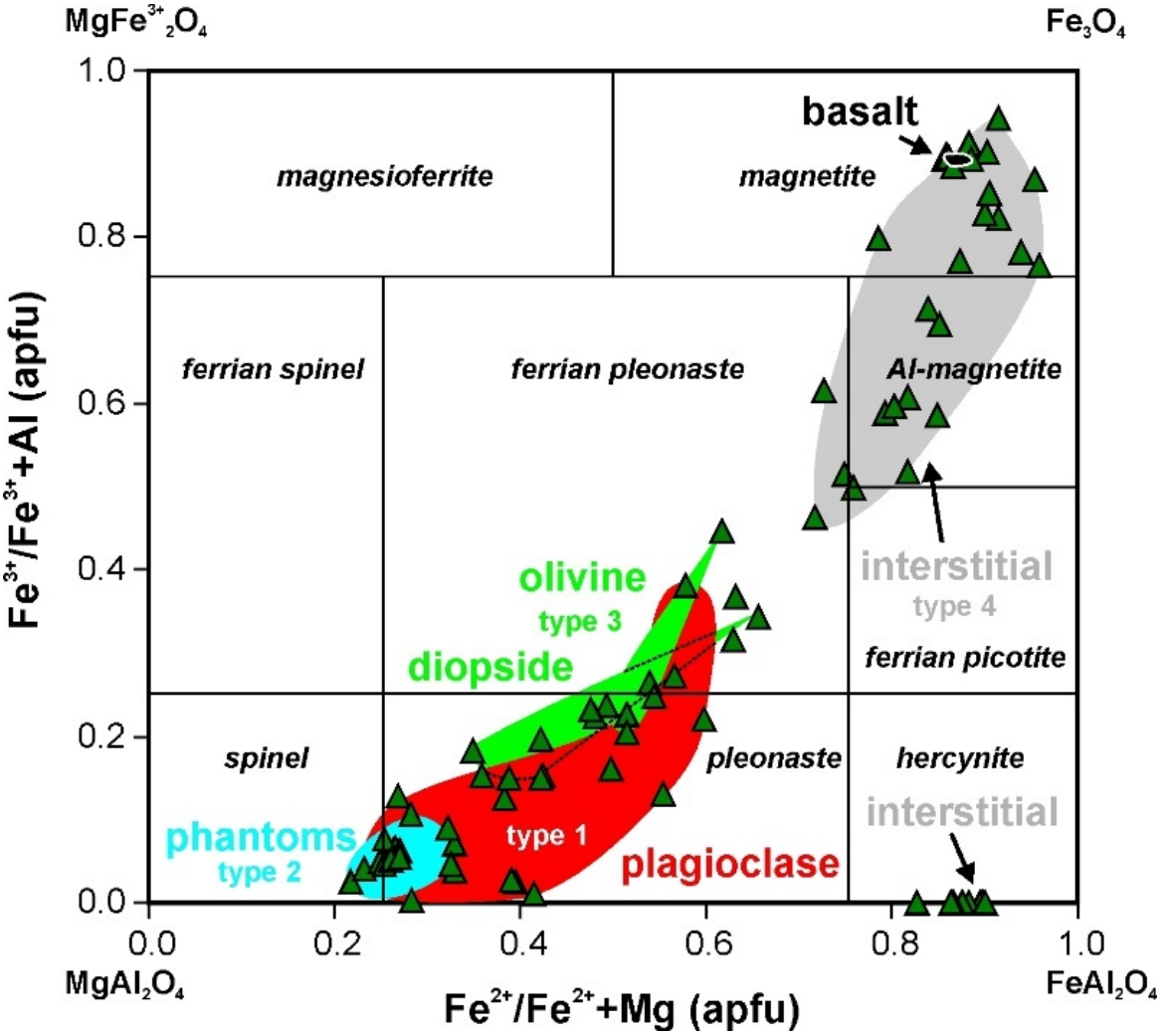

Figure 14. Classification diagram for the spinel group minerals form Čamovce, representing the lateral-left face projection of the multicomponent prism defined by spinel, hercynite, chromite, magnesiochromite, magnesioferrite and magnetite endmembers [40]. Phase boundaries are from [41,42].

Early spinel in anorthite layers corresponds to Mg,Al-spinel, less frequently to hercynite, and very rarely to magnetite. The extensive compositional range probably comprises several spinel types. In general, however, the large homogeneous rock-forming spinels (Figure 4C) correspond to Mg,Al-spinel, which is only slightly more magnesian than small spinels associated with olivines in pseudomorphs, showing the most aluminoan composition with up to 76.2 mol% $MgAl_2O_4$. On the other side, more ferroan type 1 spinels overlap the field of type 3 spinel inclusions in diopside, esseneite and olivine II. It should be noted that the hercynian spinels also occur in pseudomorphs, where they can be distinguished from dominant Mg,Al-spinels only in X-ray maps (Figure 10). The interstitial spinel-group minerals belong invariably to the magnetite-ulvöspinel series, overlapping the compositional field of Fe,Ti-oxide phenocrysts in the surrounding basalt. Hercynite with appreciable amounts of chromite-magnesiochromite (27–30 mol%) is enclosed in plagioclase in xenolith Cam-031. Increased concentrations of the Cr-rich components, up to 7.5 mol%, also occur in spinels associated with Al,Fe^{3+}-rich clinopyroxenes in sample Cam-14 (Figure 9).

4.3.7. Rhombohedral Fe,Ti-Oxides

Ilmenite occurs in mafic spindles in the proximity or direct contact with olivine crystals protruding into carbonate clusters. Ilmenite crystals, 1–20 μm wide and 50–200 μm long, occasionally contain silicate melt inclusions. Some crystals are fractured. Compositions of

the carbonate-bound ilmenites are similar in all xenoliths, showing appreciable amounts of magnesium stored in the geikielite component. The ilmenites plot along the ilmenite-hematite join, showing 0–16 mol% hematite component (Figure 15). Ilmenite in the xenolith Ca-22 is more oxidized (9.2 mol% Fe_2O_3 in average) and contains less $MgTiO_3$ (23 mol% in average) compared to the other two samples, which contain 26.6 mol% $MgTiO_3$ and 4.5 mol% Fe_2O_3 in average.

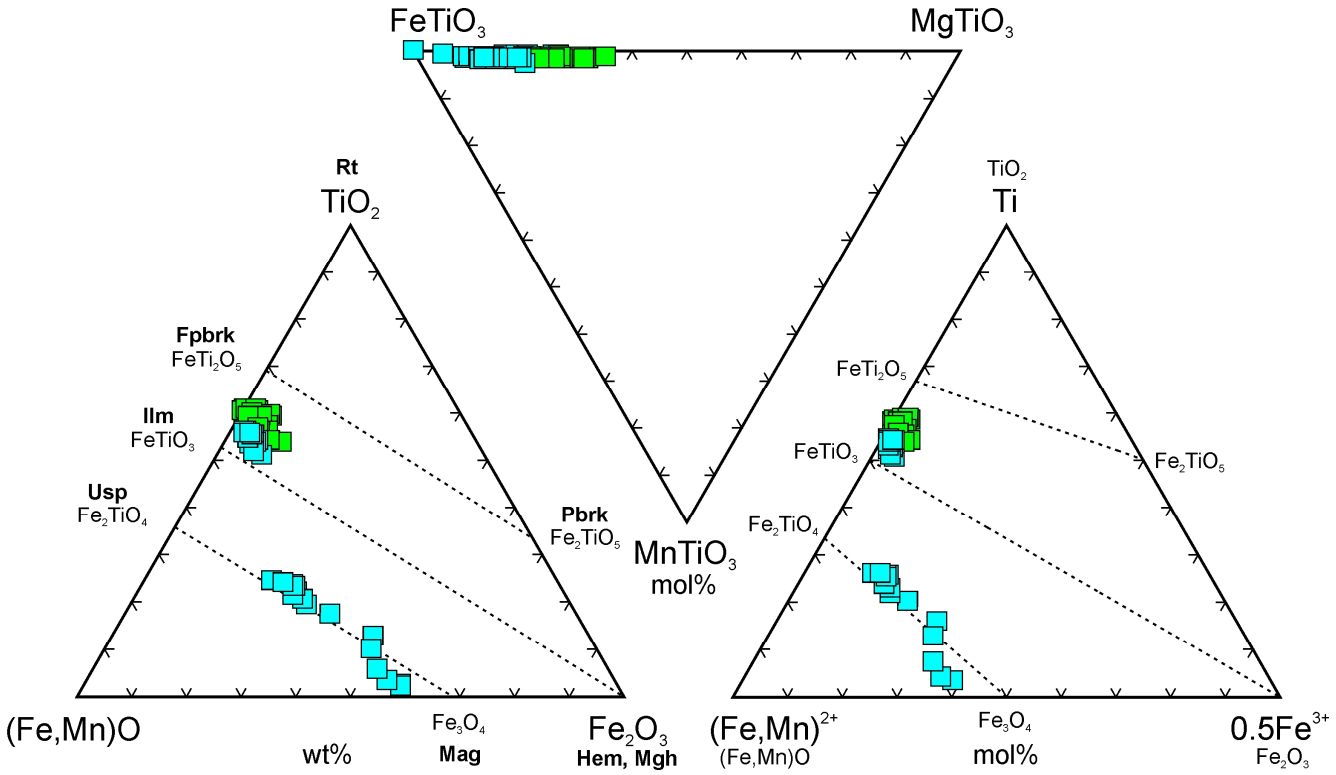

Figure 15. General classification schemes of oxyspinels and ilmenite [43] with projection points of ilmenite and ulvöspinel-magnetite from Čamovce xenoliths. Green symbols—ilmenites associated with olivine in carbonates, blue symbols—basalt phenocrystic and xenolith interstitial alkalic metasomatic assemblages.

Ilmenite also crystallized together with titanomagnetite and ulvöspinel in intergranular spaces as a member of the alkali metasomatic paragenesis. Composition of these ilmenites is similar to phenocrystic groundmass ilmenites in alkali basalt host. The ilmenites are characterized by a decreased amount of geikielite (10–18 mol%) component and occur only in xenoliths Ca-21B and Ca-10 B.

4.3.8. Melilite

The Al,Fe^{3+}-rich pyroxenes rarely contain irregularly distributed melilite inclusions (Figure 8C, Table 3) defined as åkermanite due to the prevalence of ferro- and alumo-åkermanite (45–83 mol%) over gehlenite, although some analyses project in the gehlenite field in the Ca+Na+K versus Al^{VI} versus Mg classification diagram (Figure 16A,B). The melilites from Čamovce are further typical of a non-linear coupled $Fe^{3+} + Al^{3+} = Si^{4+} + R^{2+}$ substitution (Figure 16C), also described in melilites from coal-fire buchite [2], paralavas [2,7] and skarns [7,44]. Generally, the composition of melilite from Čamovce is consistent with that occurring in paralavas of Central Appenines [45].

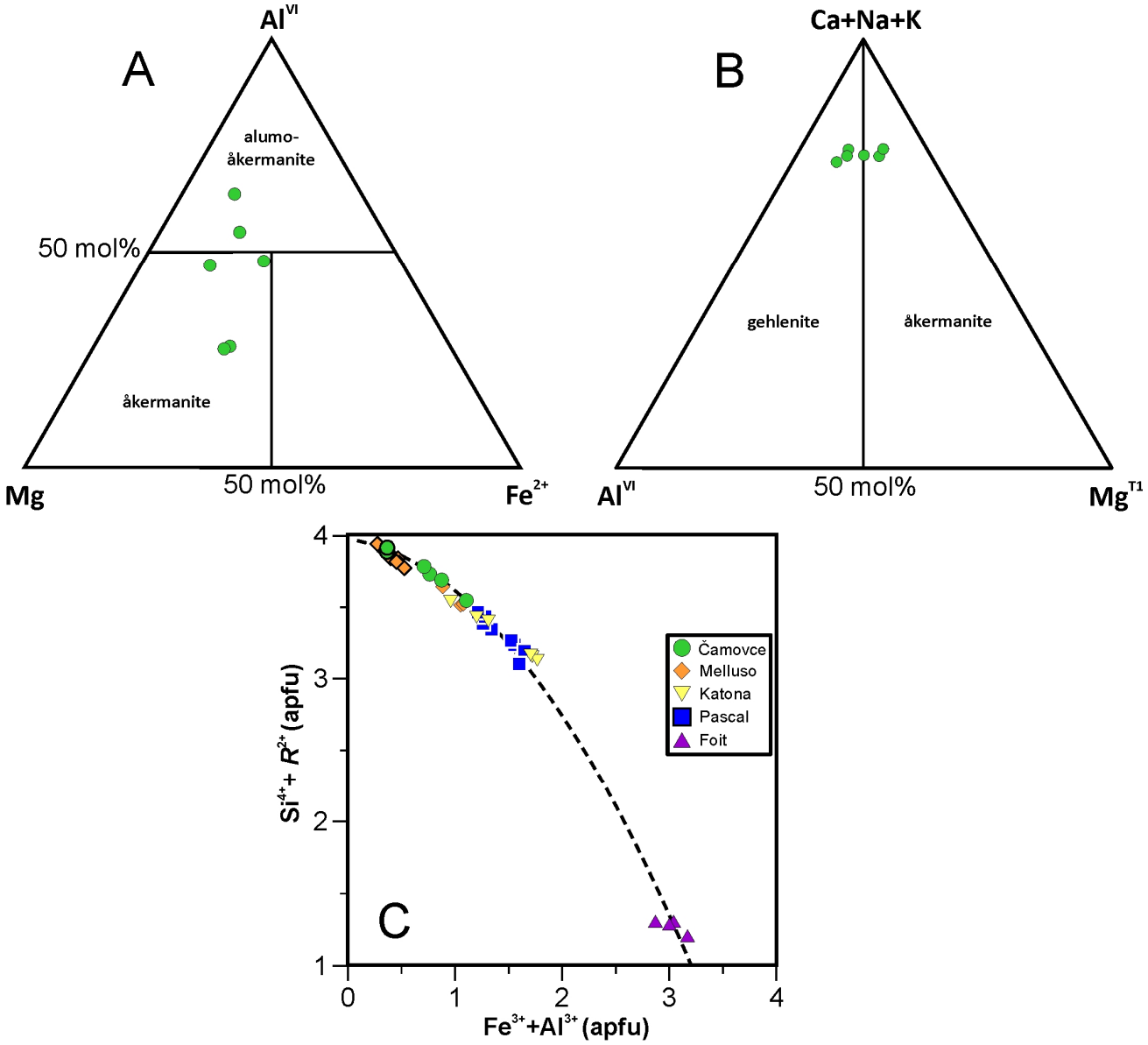

Figure 16. (**A**,**B**) Classification diagrams of melilite-group minerals from Čamovce; (**C**) Fe^{3+} +Al^{3+} versus Si^{4+} +R^{2+} diagram and comparison with literature data [2,44,45,47]. R^{2+} denotes divalent cations.

4.4. Thermobarometry

A plethora of thermobarometers is theoretically available to constrain formation *P-T* conditions of the mineral association in calc-silicate xenoliths from Čamovce. Potential applications involve thermometers based on minor element concentrations (Al, Cr, V) in olivine [48,49], exchange of Al and Cr between coexisting olivine-spinel [50,51], and Ca between olivine and clinopyroxene [52]. For the trace element-based applications, however, EPMA is an unsuitable method owing to insufficient sensitivity and detection limits resulting in the large spread and unsystematic behavior of these elements in xenoliths studied. For instance, Al and Cr concentrations in olivines range from detection limit up to 900 ppm, indicating the electron beam-induced phase-boundary fluorescence from neighboring Ca-plagioclase and/or Mg,Al-spinel. The Al-Cr exchange thermometer [50] applied to larger spinel and olivine grains also returned unrealistically high temperatures, often exceeding 1500 °C. The general trend of positively correlated Ca and Fe contents in the olivines may reflect a temperature control, but the mineral association (missing orthopy-

roxene, obvious disequilibrium with neighboring clinopyroxene) and forsterite contents below the calibration range of olivine-clinopyroxene thermometer (Fo >88 mol%) precludes reliable temperature determination. Extremely high Ca concentrations in olivines, from 1400 to 4700 ppm, reflect the combined effect of the metasomatism in Ca-rich environment and the phase-boundary fluorescence, which generally overestimates the *P-T* parameters inferred from calibrations based on olivines and spinels from non-metasomatized mantle rocks.

Table 3. Representative EPMA analyses, crystal chemistry and endmembers of melilite.

Sample	Ca-14	Ca-14	Ca-14	Ca-14	Ca-14	Cam-14
Analysis #	**49**	**56**	**57**	**61**	**86**	**10**
SiO_2 (wt%)	41.40	40.91	36.34	32.69	37.25	35.73
TiO_2	0.01	b.d.l.	0.02	0.02	0.02	0.04
Al_2O_3	6.70	6.13	13.42	19.07	11.37	14.78
Cr_2O_3	0.02	0.05	0.02	0.05	0.02	0.01
FeO	7.10	7.33	6.47	3.98	5.28	5.44
NiO	0.01	b.d.l.	b.d.l.	0.01	b.d.l.	0.01
MnO	0.15	0.21	0.26	0.09	0.14	0.11
MgO	6.61	6.55	3.85	3.65	5.43	4.13
CaO	36.39	37.04	37.56	38.03	36.55	36.77
K_2O	0.03	0.03	b.d.l.	0.02	0.04	0.03
Na_2O	1.89	1.87	1.72	1.51	2.17	2.14
Total	100.30	100.12	99.66	99.12	98.26	99.20
Si (apfu)	1.918	1.901	1.696	1.517	1.745	1.660
Ti	0.000	0.000	0.001	0.001	0.001	0.001
Al^{IV}	0.082	0.099	0.304	0.483	0.255	0.340
Al^{VI}	0.284	0.237	0.434	0.560	0.373	0.470
Cr	0.001	0.002	0.001	0.002	0.001	0.000
Fe^{3+} *	0.000	0.030	0.025	0.058	0.079	0.062
Fe^{2+}	0.275	0.255	0.228	0.096	0.128	0.150
Ni	0.000	0.000	0.000	0.000	0.000	0.001
Mn	0.006	0.008	0.010	0.004	0.005	0.004
Mg	0.456	0.454	0.268	0.252	0.379	0.286
Ca	1.806	1.844	1.878	1.890	1.844	1.831
K	0.002	0.002	0.000	0.001	0.002	0.002
Na	0.169	0.168	0.156	0.136	0.197	0.193
Na-melilite ** (mol%)	17.4	16.6	15.1	13.2	19.1	18.8
Gehlenite	1.5	0.0	24.7	42.2	13.5	24.2
Åkermanite	50.6	51.2	31.0	27.6	43.6	32.7
Fe-åkermanite	30.5	32.2	29.2	16.9	23.8	24.2

b.d.l.—below detection limit; * calculated from stoichiometry; ** calculated after [46].

Exchange and net transfer of major elements are more robust thermobarometric methods to constrain formation *P-T* conditions, as the elemental concentrations exceeding several wt% of oxide are only marginally affected by the phase-boundary fluorescence. The olivine-ilmenite thermometer [53,54] appears to be a plausible model because the ilmenite and geikielite components in ilmenite and forsterite content in olivine can be easily determined by EPMA. Moreover, the thermometer is calibrated to a wide range of temperatures (700–1300 °C) and pressures (from 100 kPa to 5.7 GPa), and ilmenite and olivine create well-developed crystals inside carbonate groundmass in our xenoliths, thus indicating equilibrium crystallization. EPMA data on the ilmenite-olivine pairs together with temperatures calculated for pressures of 1 and 2 GPa are listed in Tables 4 and 5. The olivine-ilmenite thermobarometer is univariant and should be combined with an independent thermo- or barometer. In our case, the necessary constraint is provided by calcite-aragonite stability boundary, which defines the lower limit for crystallization *PT* conditions.

Table 4. EPMA analyses (wt% oxides) of ilmenites coexisting with olivines.

Sample						**Cam-13**						**Cam-15**				**Ca-22**		
Analysis	**1**	**12**	**15**	**17**	**19**	**61**	**37**	**39**	**41**	**43**	**45**	**6**	**10**	**2**	**4**	**6**	**10**	**14**
SiO_2	b.d.l.	0.33	0.08	0.08	b.d.l.	0.07	0.03	0.07	0.02	0.05	0.05	0.51	0.04	0.09	0.11	0.07	0.46	0.11
TiO_2	53.80	55.01	55.31	54.51	54.68	53.15	54.53	54.38	55.30	55.26	54.70	53.09	53.50	53.73	53.74	51.61	51.45	52.58
Al_2O_3	0.11	0.20	0.04	0.04	0.13	0.04	0.05	0.03	0.07	0.09	0.04	0.07	0.07	0.06	0.05	0.05	0.26	0.06
Cr_2O_3	b.d.l.	0.04	0.01	b.d.l.	b.d.l.	0.05	0.02	b.d.l.	0.05	0.02	0.02	0.05	b.d.l.	0.39	0.07	0.03	0.01	0.00
V_2O_3	0.07	0.10	0.28	0.16	0.13	0.08	0.07	0.21	0.27	0.26	0.22	0.06	0.08	0.10	0.17	0.01	0.14	0.16
Fe_2O_3	3.77	b.d.l.	b.d.l.	1.73	2.55	4.07	32.56	35.49	35.66	34.62	32.79	30.81	30.81	32.53	34.71	33.60	34.55	34.63
FeO	33.13	34.57	35.27	34.63	34.08	34.16	2.51	1.19	0.00	0.44	2.17	5.11	4.59	3.46	1.59	6.22	4.69	4.20
NiO	n.a.	n.a.	n.a.	n.a.	n.a.	b.d.l.	n.a.	n.a.	n.a.	n.a.	n.a.	0.01	0.02	0.02	0.07	b.d.l.	b.d.l.	0.02
ZnO	b.d.l.	b.d.l.	b.d.l.	b.d.l.	b.d.l.	0.04	0.02	0.02	0.03	b.d.l.	0.01	b.d.l.	0.01	0.02	0.03	0.05	0.02	0.00
MnO	0.54	0.53	0.69	0.55	0.60	0.72	0.57	0.59	0.49	0.60	0.49	0.52	0.63	0.76	0.74	0.73	0.64	0.73
MgO	7.53	7.74	7.20	7.24	7.46	6.89	8.30	6.68	7.37	7.95	8.54	9.12	9.31	8.22	7.13	6.76	6.43	6.68
CaO	1.04	0.35	0.26	0.82	0.95	0.57	0.91	0.78	0.29	0.30	0.61	0.65	0.12	0.38	0.16	0.15	0.18	0.13
Total	100.00	98.88	99.13	99.75	100.57	99.84	99.57	99.44	99.55	99.58	99.64	100.00	99.18	99.77	98.58	99.28	98.83	99.30
Ilmenite Formula Based on 3 O and 2 Cations																		
Si (apfu)	0.000	0.008	0.002	0.002	0.000	0.002	0.001	0.002	0.001	0.001	0.001	0.012	0.001	0.002	0.003	0.002	0.011	0.003
Ti	0.964	0.993	1.002	0.980	0.974	0.959	0.975	0.985	0.996	0.991	0.976	0.940	0.956	0.961	0.980	0.939	0.940	0.956
Al	0.003	0.006	0.001	0.001	0.004	0.001	0.001	0.001	0.002	0.003	0.001	0.002	0.002	0.002	0.001	0.001	0.008	0.002
Cr	0.000	0.001	0.000	0.000	0.000	0.001	0.000	0.000	0.001	0.000	0.000	0.001	0.000	0.007	0.001	0.001	0.000	0.000
V	0.001	0.002	0.005	0.003	0.002	0.001	0.001	0.004	0.005	0.005	0.004	0.001	0.001	0.002	0.003	0.000	0.003	0.003
Fe^{3+}	0.068	0.000	0.000	0.031	0.046	0.074	0.045	0.022	0.000	0.008	0.039	0.091	0.082	0.062	0.029	0.113	0.086	0.076
Fe^{2+}	0.660	0.694	0.710	0.692	0.675	0.685	0.647	0.715	0.714	0.690	0.651	0.606	0.612	0.647	0.703	0.680	0.702	0.700
Ni	0.000	0.000	0.000	0.000	0.000	0.000	0.000	0.000	0.000	0.000	0.000	0.000	0.000	0.000	0.001	0.000	0.000	0.000
Zn	0.000	0.000	0.000	0.000	0.000	0.001	0.000	0.000	0.000	0.000	0.000	0.000	0.000	0.000	0.001	0.001	0.000	0.000
Mn	0.011	0.011	0.014	0.011	0.012	0.015	0.011	0.012	0.010	0.012	0.010	0.010	0.013	0.015	0.015	0.015	0.013	0.015
Mg	0.267	0.277	0.259	0.258	0.263	0.246	0.294	0.240	0.263	0.282	0.302	0.320	0.330	0.291	0.258	0.244	0.233	0.241
Ca	0.026	0.009	0.007	0.021	0.024	0.015	0.023	0.020	0.007	0.008	0.016	0.017	0.003	0.010	0.004	0.004	0.005	0.003
Ilmenite Endmember Mole Fractions *																		
Ilmenite	0.663	0.715	0.733	0.706	0.686	0.682	0.656	0.732	0.731	0.704	0.656	0.596	0.598	0.647	0.710	0.656	0.688	0.688
Geikielite	0.269	0.285	0.267	0.263	0.268	0.245	0.298	0.246	0.269	0.288	0.305	0.315	0.322	0.291	0.260	0.235	0.228	0.237

b.d.l.—below detection limit, n.a.—not analyzed; * Hematite = 1 − Geikielite − Ilmenite.

Table 5. EPMA analyses (wt% oxides) of olivines coexisting with ilmenites (Table 4) and thermobarometric data calculated after [53,54].

Sample						**Cam-13**							**Cam-15**				**Ca-22**		
Analysis	**2**	**11**	**16**	**18**	**20**	**60**	**38**	**40**	**42**	**44**	**46**	**5**	**9**	**1**	**3**	**5**	**9**	**13**
SiO_2	38.37	38.56	38.77	38.21	38.67	38.51	39.36	38.75	38.88	38.74	38.85	39.04	39.40	39.11	38.78	38.32	38.77	38.02
TiO_2	0.06	n.a.	n.a.	n.a.	n.a.	0.07	0.01	0.06	0.11	0.04	0.11	0.06	0.02	0.02	0.02	0.02	0.06	0.01
Al_2O_3	0.03	0.10	0.01	0.01	0.02	0.04	0.00	0.01	0.03	0.02	0.02	b.d.l.	0.02	0.02	0.08	0.10	0.08	0.03
Cr_2O_3	b.d.l.	b.d.l.	b.d.l.	b.d.l.	b.d.l.	b.d.l.	0.01	b.d.l.	b.d.l.	0.01	0.01	b.d.l.	b.d.l.	b.d.l.	b.d.l.	0.02	b.d.l.	0.01
Fe_2O_3	1.82	2.16	1.50	1.37	1.46	1.57	0.92	0.91	1.13	1.75	2.25	1.21	1.48	1.26	0.28	0.64	1.14	2.32
FeO	18.43	17.91	18.10	18.91	19.09	20.23	17.91	19.08	18.22	17.66	15.99	16.95	15.92	18.05	19.31	19.10	18.81	18.75
NiO	0.05	0.05	0.05	0.05	0.05	0.05	0.02	0.05	0.01	0.05	0.05	0.06	0.06	0.10	0.08	0.09	0.07	0.08
MnO	0.34	0.30	0.33	0.32	0.35	0.47	0.29	0.32	0.27	0.28	0.25	0.30	0.29	0.34	0.33	0.33	0.29	0.31
MgO	41.11	41.24	41.71	40.48	40.97	40.23	42.52	41.09	41.90	42.15	43.32	42.76	43.87	42.07	40.70	40.34	41.16	40.37
CaO	0.42	0.95	0.40	0.39	0.46	0.35	0.31	0.34	0.29	0.30	0.32	0.34	0.32	0.30	0.38	0.36	0.52	0.39
Total	100.62	101.28	100.88	99.74	101.07	101.53	101.35	100.62	100.83	101.01	101.18	100.73	101.38	101.28	99.96	99.33	100.89	100.30
Olivine Formula Based on 4 O and 3 Cations																		
Si (apfu)	0.981	0.979	0.986	0.987	0.986	0.983	0.992	0.990	0.988	0.982	0.977	0.988	0.986	0.989	0.997	0.992	0.988	0.978
Ti	0.001	0.000	0.000	0.000	0.000	0.001	0.000	0.001	0.002	0.001	0.002	0.001	0.000	0.000	0.000	0.000	0.001	0.000
Al	0.001	0.003	0.000	0.000	0.001	0.001	0.000	0.000	0.001	0.001	0.001	0.000	0.001	0.001	0.003	0.003	0.002	0.001
Cr	0.000	0.000	0.000	0.000	0.000	0.000	0.000	0.000	0.000	0.000	0.000	0.000	0.000	0.000	0.000	0.000	0.000	0.000
Fe^{3+}	0.035	0.041	0.029	0.027	0.028	0.030	0.017	0.018	0.022	0.033	0.043	0.023	0.028	0.024	0.005	0.013	0.022	0.045
Fe^{2+}	0.394	0.380	0.385	0.408	0.407	0.432	0.377	0.408	0.387	0.374	0.336	0.359	0.333	0.382	0.415	0.414	0.401	0.404
Ni	0.001	0.001	0.001	0.001	0.001	0.001	0.000	0.001	0.000	0.001	0.001	0.001	0.001	0.002	0.002	0.002	0.002	0.002
Mn	0.007	0.007	0.007	0.007	0.008	0.010	0.006	0.007	0.006	0.006	0.005	0.006	0.006	0.007	0.007	0.007	0.006	0.007
Mg	1.567	1.561	1.581	1.559	1.557	1.531	1.597	1.566	1.586	1.593	1.624	1.612	1.636	1.585	1.559	1.557	1.563	1.549
Ca	0.011	0.026	0.011	0.011	0.013	0.010	0.008	0.009	0.008	0.008	0.009	0.009	0.009	0.008	0.011	0.010	0.014	0.011
Olivine Endmember Mole Fraction																		
Fayalite *	0.215	0.213	0.207	0.218	0.218	0.232	0.198	0.214	0.205	0.204	0.189	0.191	0.181	0.204	0.212	0.215	0.213	0.225
T (°C) at 1 GPa	780	775	705	754	775	771	785	695	703	757	767	819	798	796	728	724	695	737
T (°C) at 2 GPa	815	822	748	794	813	805	824	733	747	801	807	855	834	833	767	754	725	769

b.d.l.—below detection limit, n.a.—not analyzed; * Forsterite = 1 − Fayalite.

The discovery of tschermakite in pseudomorphs extends the spectrum of possible thermobarometric applications towards the plagioclase-amphibole net-transfer and exchange equilibria (e.g., [55–58]), as well as Al-in-amphibole empirical barometers for calc-alkaline magmatic and metamorphic rocks (e.g., [59–62]). The amphibole-only thermobarometer [63] was primarily designed to constrain amphibole saturation temperatures in hydrous melts and seems thus to be irrelevant in this study.

Although the equilibrium NaSi-CaAl exchange-based calibrations also involve tschermakite component, they are not applicable to the quartz-free assemblage of Čamovce xenoliths, except for the most recent calibration [57], which also covers magmatic and metamorphic amphiboles with high Al^{VI} occupancy in silica-undersaturated rocks. The amphibole #9 (Table 2) combined with the most basic $An_{87.5}$ plagioclase from Figure 10, overlapping the compositional range of other rock-forming plagioclases, returns 781 ± 13 °C and 2.05 ± 0.03 GPa. It should be emphasized, however, that the other amphibole analysis with incomplete C-site occupancy listed in Table 2 does not meet strictly prescribed compositional criteria of reliable *PT* calculation. Various popular empirical models cited above based on the total Al content calculated from crystal formula with 23 oxygen atoms also indicate increased formation pressures, between 1.27 and 1.95 GPa.

5. Discussion

5.1. Protolith

Primary magmatic, metamorphic or mixed origins can be deduced from the observed fabric and textures of xenoliths from Čamovce revealed by CT and optical microscopy. Ultramafic rocks often exhibit banded texture resulting from the magmatic crystallization and differentiation of mineral fractions. In our case, however, the alternating layers create spindles rather than two-dimensional bands. Intercalations of plagioclase-rich layers due to injection of neosom along existing foliation are typical of migmatites, and the observed banded texture is principally similar to that in migmatites. In our case, however, very thin layering is rather curious. Distinctive planar anisotropy and augen structure locally detected in our samples is also typical of gneiss. The contact of lensoidal aggregates with surrounding rock is sharp and they are probably the youngest phenomena originating in the conditions of pure shear. In general, the texture of our xenoliths displays features typical of the mylonitic fabric with mafic layers disintegrated and stretched to small-flattened lenses strongly elongated in the direction of stretching. Asymmetric structures have not been detected in macroscopic scale, so the pure shear flattening was dominant. Based on the macroscopic character, we interpret the Čamovce xenoliths as strongly flattened and stretched (mylonitized), banded micro-migmatite.

High Cr contents in spinels (up to 30 mol% chromite/magnesiochromite) and abundant Cu-sulfides predating the rock-forming spinel indicate a mafic magmatic precursor similar to lunar Al-rich spinel anorthosites [64,65], or terrestrial Archean layered intrusions [66,67]. Some xenoliths from Čamovce dominated by olivine in Ca-plagioclase groundmass (e.g., Figure 3D) are reminiscent of troctolites. On the other hand, the discovery of tschermakite strongly implies a sedimentary protolith, as the extremely Al-rich amphiboles are minerals diagnostic of metamorphosed marbles [38,68] or contacts of anorthosites with amphibolites [69]. Apart from the high Al^{VI}, between 1.95 and 2.1 apfu, which approaches the maximum postulated by [70], the amphibole from Čamovce is also characterized by the very low occupancy of the A-site (<0.1 apfu)—the feature thought to be diagnostic of high-pressure metamorphic rocks [71].

The Ca + Al + Mn versus Ti + V discrimination diagram (Figure 17) demonstrates that rock-forming and pseudomorph Mg-Al spinels project within the skarn field, whereas the interstitial Fe-Ti spinels of the magnetite-ulvöspinel supergroup are similar to those from magmatic porphyry and Kiruna-type deposits. Considering the composition and micro-textural context, the Ti-magnetite and associated apatite, biotite, sodalite, nepheline and K-feldspar can be linked with the late metasomatic alteration during interaction with surrounding basalt.

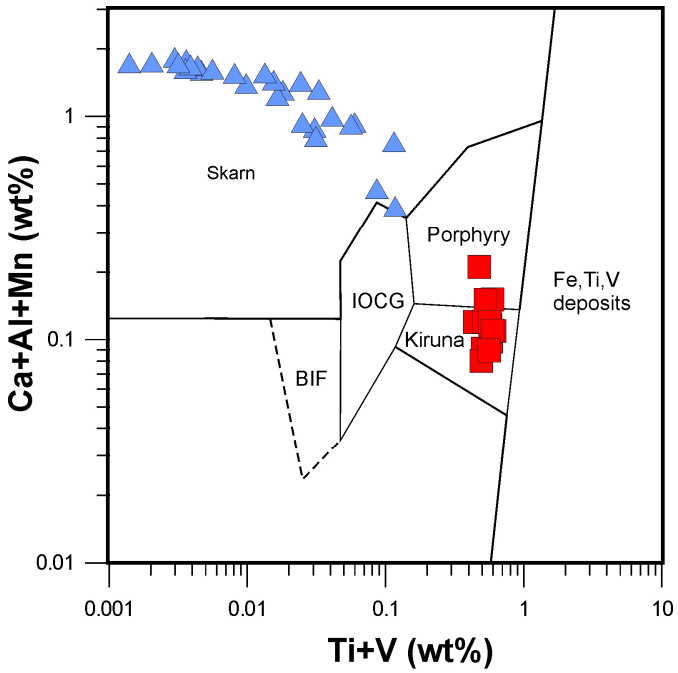

Figure 17. Genetic discrimination diagram of Fe,Ti,Mg-oxides [72] based on Ca+Al+Mn and Ti+V contents in spinels (blue triangles) and ulvöspinel-magnetite series (red squares) from Čamovce xenoliths. Abbreviations: BIF—Banded iron formations, IOCG—Iron oxide copper-gold deposits.

5.2. P-T Constraints on the Stability of Tschermakite, Kushiroite and Esseneite

Tschermakite breakdown has been studied along the tschermakite-ferritschermakite join in the temperature range of 750–1000 °C, and pressures between 0.5 and 2.4 GPa in the presence of vapor [73]. Pure tschermakite is stable up to 800 °C between 0.7 and 1.7 GPa, and ~900 °C at ~1.1 GPa. At high pressures, tschermakite breaks down to high-Al tschermakitic amphibole coexisting with garnet and quartz. At intermediate pressures between 1.2–1.5 GPa, tschermakite decomposes to high-Al amphibole, clinopyroxene, orthopyroxene and quartz. Silica-undersaturated assemblages with anorthite, orthopyroxene, clinopyroxene or anorthite, orthopyroxene and forsterite are stable below 1.1 GPa. $MgAl_2O_4$ spinel is stable at temperatures higher than 930 °C.

The experimental tschermakite stability limit at high pressure was defined by the reaction:

$$\text{Tschermakite} = \text{Garnet} + \text{Diopside} + \text{Kyanite} + H_2O$$

$$Ca_2Mg_3Al_4Si_6O_{22}(OH)_2 = CaMg_2Al_2Si_3O_{12} + CaMgSi_2O_6 + Al_2SiO_5 + H_2O$$

The following reaction was proposed to account for the observed low-pressure experimental assemblage:

$$\text{Tschermakite} = \text{Forsterite} + 2\text{Anorthite} + \text{orthopyroxene} + H_2O$$

$$Ca_2Mg_3Al_4Si_6O_{22}(OH)_2 = Mg_2SiO_4 + 2CaAl_2Si_2O_8 + MgSiO_3 + H_2O$$

The presence of trivalent iron shifted the stability field of Al,Fe^{3+}-rich amphibole associated with orthopyroxene, clinopyroxene and Fe-oxides (magnetite, hematite) to higher temperature and pressure. At 850 °C and 2.0 GPa, Al,Fe^{3+}-rich amphibole breaks down to garnet, clinopyroxene, orthopyroxene and Fe-oxides, whereas the high-temperature, intermediate pressure assemblage consisted of clinopyroxene, orthopyroxene, Fe-oxides and olivine, the latter replaced by anorthite below 1.2 GPa. Simplified phase relations together with compositions of Al-rich amphiboles coexisting with garnet are depicted in Figure 18.

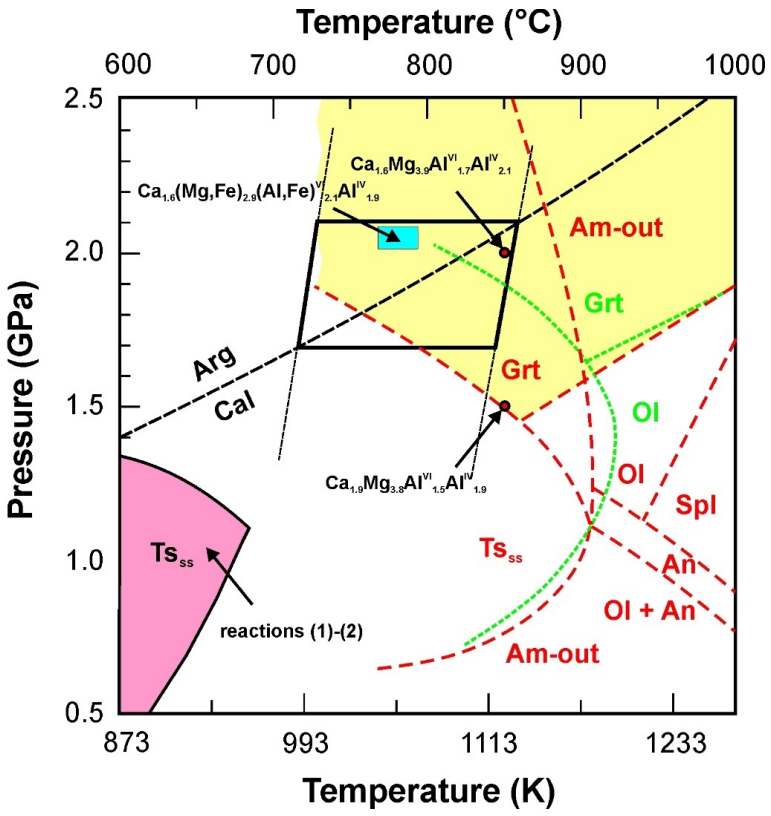

Figure 18. Summary of *PT* constraints obtained from the ilmenite-olivine thermometer [53,54] (trapezoid area), equilibrium coordinates of reactions (1) and (2) calculated for various XCO_2 values (pink area), calcite-aragonite stability boundary (diagonal thick-dashed curve), plagioclase-amphibole thermobarometer [57] (blue square) applied to amphibole (analysis #9, Table 2) coexisting with $An_{87.5}$ plagioclase, and phase boundaries inferred from experimental data [73] (green stippled curves for ferritschermakite, red dashed curves for tschermakite sensu stricto—Ts_{ss}). Red dots indicate compositions of Al-rich amphiboles coexisting with garnet at 1.5 and 2.0 GPa [73]. Thermodynamic calculations were made using the PERPLE_X 07 program [74,75], pure compounds involved in thermodynamic database [76], and compensated-Redlich–Kwong equation of state (CORK EOS) for H_2O-CO_2 fluids adapted for high pressures [77]. Mineral abbreviations [30]: Am—amphibole, An—anorthite, Arg—aragonite, Cal—calcite, Grt—garnet, Ol—olivine, Spl—spinel.

Tschermakite breakdown during dehydration and decarbonatization of calc-silicate rocks at various XCO_2 can be quantitatively modeled using the following reactions taking place at lower and higher pressures, respectively:

$$\begin{gathered}\text{Tschermakite} + CaCO_3 = 2\text{Diopside} + \text{Anorthite} + \text{Spinel} + H_2O + CO_2 \\ Ca_2Mg_3Al_4Si_6O_{22}(OH)_2 + CaCO_3 = 2CaMgSi_2O_6 + CaAl_2Si_2O_8 + MgAl_2O_4 + H_2O + CO_2\end{gathered} \quad (1)$$

$$\begin{gathered}\text{Tschermakite} + MgCO_3 + \text{Quartz} = \text{Pyrope} + \text{Diopside} + \text{Anorthite} + H_2O + CO_2 \\ Ca_2Mg_3Al_4Si_6O_{22}(OH)_2 + MgCO_3 = Mg_3Al_2Si_3O_{12} + CaMgSi_2O_6 + CaAl_2Si_2O_8 + H_2O + CO_2\end{gathered} \quad (2)$$

Thermodynamic modeling of reactions (1) and (2) using pure compounds indicates the tschermakite stability at lower pressure and temperature compared to experiments (Figure 18), but also documents the shift of the stability field to higher pressures and lower temperatures with increasing CO_2 contents.

It should be emphasized that none of the reactions proposed above fully reproduces the mineral assemblage of pseudomorphs in Čamovce xenoliths. Garnet, quartz and orthopyroxene have not been detected, although the PT parameters constrained by the plagioclase-amphibole thermobarometry project within the garnet stability field. On the other side, olivine and spinel are experimental tschermakite breakdown products at inter-

mediate pressures and increased temperatures. The olivine-spinel-plagioclase assemblage of pseudomorphs does not create typical symplectites, but rather indicates the crystallization sequence from early dendritic spinel formed by rapid cooling, through euhedral olivine with spinel inclusions, to interstitial intermediate to ternary plagioclase, similar to that associated with ilmenite and olivine in carbonate pockets. The columnar olivine habit is common in rocks that underwent rapid cooling [78].

The stability of esseneite and kushiroite is strongly dependent on the oxygen fugacity. In reducing conditions, the esseneite becomes unstable and decomposes to garnet and spinel [79–82]. In oxidizing conditions, however, the garnet was synthesized only at very high pressure and temperature, 3.5 GPa and 1330 °C [79], as a product of the Fe^{3+} and Al ordering between tetrahedral and octahedral sites [80].

Melilite is another important indicator of high-temperature thermo-metamorphism of silica-undersaturated igneous rocks, occurring in an increased oxygen fugacity environment [1,2,81]. One of the possible reactions involving esseneite, melilite and anorthite is as follows:

$$\text{Anorthite} + \text{Gehlenite} + \text{Magnetite} + O_2 = \text{Esseneite} + \text{Hercynite}$$

However, diopside relics in centers of larger pyroxene grains together with typical diffusion profiles and textures controlled by phase boundaries (Figures 8 and 9) suggest the Al,Fe^{3+}-rich pyroxene formation during a high-temperature elemental exchange between diopside-augite and oxidizing carbonate-silicate melt, taking place around the calcite-aragonite stability boundary. The high Fe^{3+} content in the infiltrating CO_2-oversaturated melt could account for the crystallization of Al,Fe^{3+}-rich pyroxenes, olivine and spinel at the expense of garnet. Close genetic relationship of the tschermakite breakdown and the carbonatite-silicate metasomatism is also indicated by negligible variations in olivine compositions characterized by increased Ca contents. Similar are also the compositions of plagioclases protruding into carbonate pockets and those occurring in pseudomorphs, both characterized by increased Fe^{3+} contents. Coexistence of the silicate and carbonatite melt fractions is documented by the crystallization of olivine II and ilmenite within carbonate pockets, Fe^{3+}, K-Na-Ca diffusion gradients in the rock-forming plagioclase around the carbonate pockets, and Fe-enrichment along clinopyroxene-carbonate interfaces.

The unsystematic behavior and strongly fluctuating Fe contents, from zero up to 1 wt% Fe_2O_3, in rock-forming basic plagioclases also imply diffusion rather than equilibrium crystallization condition. The increasing Fe contents and decreasing basicity of plagioclases around carbonate pockets and neoformed interstitial plagioclases may reflect combined effects of decreasing pressure and increasing oxygen fugacity documented in basic and ultrabasic plutons, Siberian traps [83] and the Bushveld complex [84].

6. Conclusions

Considering structural, mineralogical and petrological characteristics of xenoliths entrained in Pliocene basalt near Čamovce, the following conclusions can be drawn:

The macroscopic fabric of xenoliths is reminiscent of mylonitized micro-migmatites.

- The presence of Al,Fe^{3+}-rich pyroxenes with melilite inclusions testifies a thermo-metamorphic interaction of xenoliths with strongly oxidizing carbonate-aluminosilicate melt with decreased $aSiO_2$. Concentrations of the kushiroite endmember in some pyroxenes, up to 47.5 mol% (31 wt% Al_2O_3), are substantially higher than the highest natural terrestrial values known to the authors, i.e., 24 wt% in gehlenite-rich skarns from the Carpathians [7] and 22.3 wt% in exoskarn xenoliths ejected by the Merapi volcano, Indonesia [46].
- Tschermakite with high ^{VI}Al content (1.9–2.1 apfu) and very low occupancy of the A-site (<0.1 apfu), together with aragonite and calcite coexisting in carbonate pockets indicate high-pressure metamorphic conditions contradictory with other skarn xenoliths found in pyroclastic deposits [46,85,86] or layered intrusions [87] formed at pressures below 0.1 GPa. The olivine-ilmenite-aragonite-calcite and plagioclase-amphibole thermobarometers returned temperatures within the 770–860 °C range and

pressures between 1.8 and 2.1 GPa, corresponding to depths of 60–70 km assuming lithostatic load. The presence of Al,Fe^{3+} pyroxenes, forsterite and Mg,Al-spinel at the expense of garnet is a consequence of the high Al content of the parental rock, low SiO_2 activity, high CO_2 partial pressure and strongly oxidizing conditions.

- The finding of relict tschermakite in spinel-plagioclase-forsterite pseudomorphs suggest a metamorphosed calc-silicate marble originating from a sedimentary protolith. On the other hand, a magmatic protolith, similar to layered gabbro-anorthosite complexes contaminated by calcic carbonatite melt [87] cannot be ruled out considering high Cr contents in spinels and pyroxenes, abundant Cu-sulfides, and high CaO contents, 0.3–1.0 wt% CaO, in forsterite.
- Interactions between xenoliths and basalt host were dimension-dependent, showing smaller xenoliths to undergo more intense alkalic metasomatic alteration recorded by the crystallization of interstitial biotite, sanidine, sodalite, nepheline, Mg-poor ilmenite and Fe-Ti magnetite. The thermal overprint of smaller xenoliths resulted in local exsolution of corundum from basic plagioclase.

Supplementary Materials: The following supporting information can be downloaded at: https://www.mdpi.com/article/10.3390/min12020156/s1, Table S1: EPMA analyses of plagioclase; Table S2: EPMA analyses of olivine; Table S3: EPMA analyses of spinel-group minerals.

Author Contributions: Conceptualization, M.H. and L.R.; methodology, P.K., F.M. and L.R.; writing—original draft preparation, L.R.; writing—review and editing, V.H. and M.H.; project administration, M.H. and L.R. All authors have read and agreed to the published version of the manuscript.

Funding: This project was financed from the VEGA agency grants 1/0143/18, 1/0013/22 and the Comenius University of Bratislava grant UK/152/2021.

Data Availability Statement: Not applicable.

Acknowledgments: Juraj Šurka is gratefully acknowledged for the preparation of CT scans. We appreciate perceptive and thorough comments from three anonymous reviewers, which provided numerous hints, significantly improved grammar, and helped in clarifying various unclear aspects of the initial draft.

Conflicts of Interest: The authors declare no conflict of interest.

References

1. Cosca, M.; Peacor, D. Chemistry and structure of esseneite ($CaFe^{3+}AlSiO_6$), a new pyroxene produced by pyrometamorphism. *Am. Mineral.* **1987**, *72*, 148–156.
2. Foit, F.; Hooper, R.; Rosenberg, P. An unusual pyroxene, melilite, and iron oxide mineral assemblage in a coal-fire buchite from Buffalo, Wyoming. *Am. Mineral.* **1987**, *72*, 137–147.
3. Kruszewski, L.; Gatel, P.; Thiéry, V.; Moszumanska, I.; Kusy, D. Crystallochemical behavior of slag minerals and the occurrence of potentially new mineral species from Lapanouse-de-Sévérac, France. In *Coal and Peat Fires: A Global Perspective*; Stracher, G., Ed.; Elsevier: Amsterdam, The Netherlands, 2018; Volume 5, pp. 243–300.
4. Chesnokov, B.V.; Shcherbakova, E.P. *Mineralogiya gorelykh Otvalov Chelyabinskogo Ugolnogo Basseina (Opyt Mineralogii Tekhnogeneza) (Mineralogy of Burnt Dumps of the Chelyabinsk Coal Basin—Experience of Mineralogy of Technogenesis)*; Nauka: Moscow, Russia, 1991.
5. Vapnik, Y.; Sharygin, V.; Sokol, E.V. Paralavas in a combustion metamorphic complex: Hatrurim Basin, Israel. *Geol. Soc. Am. Rev. Eng. Geol.* **2007**, *18*, 1–21.
6. Yakubovich, O.V.; Zayakina, N.V.; Oleinikov, O.B.; Kostin, A.V. Esseneite from xenoliths in dacite lavas: Crystal structure and genesis. *Geol. Ore Dep.* **2019**, *61*, 689–695. [CrossRef]
7. Pascal, M.; Katona, I.; Fonteilles, M.; Verkaeren, J. Relics of high-temperature clinopyroxene on the join Di–CaTs with up to 72 mol. % Ca(Al,Fe^{3+})$AlSiO_6$ in the skarns of Ciclova and Magureaua Vatei, Carpathians, Romania. *Can. Mineral.* **2005**, *43*, 857–881. [CrossRef]
8. Kimura, M.; El Goresy, A.; Palme, H.; Zinner, E. Ca-, Al-rich inclusions in the unique chondrite ALH85085: Petrology, chemistry, and isotopic compositions. *Geochim. Cosmochim. Acta* **1993**, *57*, 2329–2359. [CrossRef]
9. Kimura, M.; Mikouchi, T.; Suzuki, A.; Miyahara, M.; Ohtani, E.; Goresy, A. Kushiroite, $CaAlAlSiO_6$: A new mineral of the pyroxene group from the ALH 85085 CH chondrite, and its genetic significance in refractory inclusions. *Am. Mineral.* **2009**, *94*, 1479–1482. [CrossRef]

10. Ma, C.; Simon, S.; Rossman, G.; Grossman, L. Calcium Tschermak's pyroxene, CaAlAlSiO6, from the Allende and Murray meteorites: EBSD and micro-Raman characterizations. *Am. Mineral.* **2009**, *94*, 1483–1486. [CrossRef]
11. Hays, J.F. Stability and properties of the synthetic pyroxene $CaAl_2SiO_6$. *Am. Mineral.* **1966**, *51*, 1524–1529.
12. Kimura, M.; El Goresy, A.; Mikouchi, T.; Suzuki, A.; Miyahara, M.; Ohtani, E. Kushiroite, $CaAl_2SiO_6$, a new mineral in carbonaceous chondrites: Its formation conditions and genetic significance in Ca-Al rich refractory inclusions. *Meteor. Planet. Sci.* **2009**, *44*, A110.
13. Konečný, V.; Kováč, M.; Lexa, J.; Šefara, J. Neogene evolution of the Carpatho-Pannonian region: An interplay of subduction and back-arc diapiric uprise in the mantle. *EGU Stephan Mueller Spec. Pub. Ser.* **2002**, *1*, 105–123. [CrossRef]
14. Downes, H.; Pantó, G.; Póka, T.; Mattey, D.; Greenwood, P. Calc-alkaline volcanics of the Inner Carpathian arc, Northern Hungary: New geochemical and oxygen isotopic results. *Acta Vulcanol.* **1995**, *7*, 29–41.
15. Dobosi, G. Late-Cenozoic alkalic basalt magmatism in northern Hungary and Slovakia: Petrology, source compositions and relationship to tectonics. *Acta Vulcanol.* **1995**, *7*, 199–207.
16. Konečný, V.; Lexa, J.; Balogh, K.; Konečný, P. Alkali basalt volcanism in Southern Slovakia: Volcanic forms and time evolution. *Acta Vulcanol.* **1995**, *7*, 167–172.
17. Vass, D.; Elečko, M. (Eds.) *Vysvetlivky ku Geologickej Mape Lučenskej Kotliny a Cerovej vrchoviny (Explanatory Notes to the Geological Map of Lučenská Kotlina Depression and Cerová Vrchovina Upland 1:50 000)*; Štátny Geologicky Ústav D. Štúra: Bratislava, Slovakia, 1992; 196p. (In Slovak)
18. Huraiová, M.; Konečný, P.; Konečný, V.; Simon, K.; Hurai, V. Mafic and salic igneous xenoliths in late Tertiary alkaline basalts: Fluid inclusion and mineralogical evidence for a deep-crustal magmatic reservoir in the Western Carpathians. *Eur. J. Mineral.* **1996**, *8*, 901–916. [CrossRef]
19. Huraiová, M.; Paquette, J.L.; Konečný, P.; Gannoun, A.M.; Hurai, V. Geochemistry, mineralogy, and zircon U–Pb–Hf isotopes in peraluminous A-type granite xenoliths in Pliocene–Pleistocene basalts of northern Pannonian Basin (Slovakia). *Contrib. Mineral. Petrol.* **2017**, *172*, 59. [CrossRef]
20. Huraiová, M.; Konečný, P.; Hurai, V. Niobium Mineralogy of Pliocene A1-Type Granite of the Carpathian Back-Arc Basin, Central Europe. *Minerals* **2019**, *9*, 488. [CrossRef]
21. Hurai, V.; Simon, K.; Wiechert, U.; Hoefs, J.; Konečný, P.; Huraiová, M.; Pironon, J.; Lipka, J. Immiscible separation of metalliferous Fe/Ti-oxide melts from fractionating alkali basalt: *P-T-f* $_{O2}$ conditions and two-liquid elemental partitioning. *Contrib. Mineral. Petrol.* **1998**, *133*, 12–29. [CrossRef]
22. Hurai, V.; Huraiová, M.; Konečny, P. REE minerals as geochemical proxies of Late-Tertiary alkalic silicate±carbonatite intrusions beneath Carpathian back-arc basin. *Minerals* **2021**, *11*, 369. [CrossRef]
23. Konečný, V.; Lexa, J.; Konečný, P.; Balogh, K.; Elečko, M.; Hurai, V.; Huraiová, M.; Pristaš, J.; Sabol, M.; Vass, D. *Guidebook to the Southern Slovakia Alkali Basalt Volcanic Field*; Štátny Geologicky Ústav D. Štúra: Bratislava, Slovakia, 2004; 143p.
24. Konečný, V. Paleogeografická Rekonštrukcia, Vulkanológia a Časová Evolúcia Cerovej Bazaltovej Formácie. In *Geológia Lučenskej kotliny a Cerovej Vrchoviny*; Vass, D., Elečko, M., Konečný, V., Eds.; Štátny Geologický Ústav D. Štúra: Bratislava, Slovakia, 2007; pp. 196–202.
25. Merlet, C. An accurate computer correction program for quantitative electron probe microanalysis. *Microchim. Acta* **1994**, *114*, 363–376. [CrossRef]
26. Åmli, R.; Griffin, W. Standards and correction factors for microprobe analysis of REE minerals. *Am. Mineral.* **1975**, *60*, 599–606.
27. Konečný, P.; Siman, P.; Holický, I.; Janák, M.; Kollárová, V. Method of monazite dating by means of the microprobe. *Miner. Slov.* **2004**, *36*, 225–235.
28. Schneider, C.; Rasband, W.; Eliceiri, K. NIH Image to ImageJ: 25 years of image analysis. *Nat. Methods* **2012**, *9*, 671–675. [CrossRef] [PubMed]
29. Ziberna, L.; Nimis, P.; Kuzmin, D.; Malkovets, V. Error sources in single-clinopyroxene thermobarometry and a mantle geotherm for the Novinka kimberlite, Yakutia. *Am. Mineral.* **2016**, *101*, 2222–2232. [CrossRef]
30. Warr, L. IMA–CNMNC approved mineral symbols. *Mineral. Mag.* **2021**, *85*, 291–320. [CrossRef]
31. Benisek, A.; Dachs, E.; Kroll, H. A ternary feldspar-mixing model based on calorimetric data: Development and application. *Contrib. Mineral. Petrol.* **2010**, *160*, 327–337. [CrossRef]
32. Morimoto, N. Nomenclature of pyroxenes. *Mineral. Petrol.* **1988**, *39*, 55–76. [CrossRef]
33. Tzvetanova, Y.; Tarassov, M.; Ganev, V.; Piroeva, I. Crystal chemistry of clinopyroxene with a high content of the Ca-Tschermak and esseneite components, Eastern Rhodopes, Bulgaria. In Proceedings of the Geonauki National Conference, Bulgarian Geological Society, Sofia, Bulgaria, 7–8 December 2016; pp. 35–36.
34. Droop, G.A. general equation for estimating Fe^{3+} concentrations in ferromagnesian silicates and oxides from microprobe analyses, using stoichiometric criteria. *Mineral. Mag.* **1987**, *51*, 431–435. [CrossRef]
35. Hattert, F.; Burke, E.A.J. The IMA-CNMNC dominant-constituent rule revisited and extended. *Can. Mineral.* **2008**, *46*, 717–728. [CrossRef]
36. Ejima, T.; Osanai, Y.; Akasaka, M.; Adachi, T.; Nakano, N.; Kon, Y.; Ohfuji, H.; Sereenen, J. Oxidation states of Fe in constituent minerals of a spinel lherzolite xenolith from Tariat Depression, Mongolia: The significance or Fe^{3+} in olivine. *Minerals* **2018**, *8*, 204. [CrossRef]

37. Locock, A.J. An Excel spreadsheet to classify chemical analyses of amphiboles following the IMA 2012 recommendations. *Comput. Geosci.* **2014**, *62*, 1–11. [CrossRef]
38. Bunch, T.E.; Okrusch, M. Al-rich pargasite. *Am. Mineral.* **1973**, *58*, 721–726.
39. Leake, B.E.; Woolley, A.R.; Arps, C.E.S.; Birch, W.D.; Gilbert, M.C.; Grice, J.D.; Hawthorne, F.; Kato, A.; Kisch, H.J.; Krivovichev, V.G.; et al. Nomenclature of amphiboles: Report of the subcommittee on amphiboles of the International Mineralogical Association, Commission on New Minerals and Mineral Names. *Can. Mineral.* **1997**, *35*, 219–246.
40. Stevens, R.E. Composition of some chromites of the western hemisphere. *Am. Mineral.* **1944**, *29*, 1–34.
41. Haggerty, S.E. Oxide mineralogy of the upper mantle. Spinel mineral group. In *Oxide Minerals: Petrologic and Magnetic Significance*; Lindsley, D.H., Ed.; Mineralogical Society of America: Chantilly, VA, USA, 1991; Volume 25, pp. 355–416.
42. Deer, W.A.; Howie, R.A.; Zussman, J. *An Introduction to the Rock-Forming Minerals*, 2nd ed.; Longman: London, UK, 1992; 696p.
43. Buddington, A.F.; Lindsley, D.H. Iron-titanium oxide minerals and synthetic equivalents. *J. Petrol.* **1964**, *5*, 310–357. [CrossRef]
44. Katona, I.; Pascal, M.L.; Fonteilles, M.; Verkaeren, J. The melilite (Gh50) skarns of Oravita, Banat, Romania: Transition to gehlenite (Gh85) and to vesuvianite. *Can. Mineral.* **2003**, *41*, 1255–1270. [CrossRef]
45. Melluso, L.; Conticelli, S.; D'Antonio, M.; Mirco, N.P.; Saccani, E. Petrology and mineralogy of wollastonite-and melilite-bearing paralavas from the Central Apennines, Italy. *Am. Mineral.* **2003**, *88*, 1287–1299. [CrossRef]
46. Whitley, S.; Halama, R.; Gertisser, R.; Preece, K.; Deegan, F.M.; Troll, V.R. Magmatic and metasomatic effects of magma-carbonate interaction recorded in calc-silicate xenoliths from Merapi volcano (Indonesia). *J. Petrol.* **2020**, *61*, egaa048. [CrossRef]
47. Pascal, M.; Fonteilles, M.; Verkaeren, J.; Piret, R.; Marincea, S. The melilite-bearing high-temperature skarns of the Apuseni Mountains, Carpathians, Romania. *Can. Mineral.* **2001**, *39*, 1405–1434. [CrossRef]
48. De Hoog, J.C.M.; Gall, L.; Cornell, D.H. Trace-element geochemistry if mantle olivine and application to mantle petrogenesis and geothermobarometry. *Chem. Geol.* **2010**, *270*, 196–215. [CrossRef]
49. Bussweiler, Y.; Brey, G.P.; Pearson, D.G.; Stachel, T.; Stern, R.A.; Hardman, M.F.; Kjarsgaard, B.A.; Jackson, S.E. The aluminium-in-olivine thermometer for mantle peridotites—Experimental versus empirical calibration and potential applications. *Lithos* **2017**, *272–273*, 301–314. [CrossRef]
50. Wan, Z.; Coogan, L.A.; Canil, D. Experimental calibration of aluminium partitioning between olivine and spinel as a geothermometer. *Am. Mineral.* **2008**, *93*, 1142–1147. [CrossRef]
51. Coogan, L.A.; Saunders, A.D.; Wilson, R.N. Aluminium-in-olivine thermometry of primitive basalts: Evidence of an anomalously hot mantle source for large igneous provinces. *Chem. Geol.* **2014**, *368*, 1–10. [CrossRef]
52. Köhler, T.P.; Brey, G.P. Calcium exchange between olivine and clinopyroxene calibrated as a geothermobarometer for natural peridotites from 2 to 60 kb with applications. *Geochim. Cosmochim. Acta* **1990**, *54*, 2375–2388. [CrossRef]
53. Andersen, D.J.; Lindsley, D.H. The olivine-ilmenite thermometer. *Lunar Planet. Sci. Conf. Proc.* **1979**, *10*, 493–507.
54. Andersen, D.J.; Lindsley, D.H. A valid Margules formulation for an asymmetric ternary solution: Revision of the olivine-ilmenite thermometer, with applications. *Geochim. Cosmochim. Acta* **1981**, *45*, 847–853. [CrossRef]
55. Blundy, J.D.; Holland, T.J.B. Calcic amphibole equilibria and a new amphibole-plagioclase geothermometer. *Contrib. Mineral. Petrol.* **1990**, *104*, 208–224. [CrossRef]
56. Holland, T.; Blundy, J. Non-ideal interactions in calcic amphiboles and their bearing on amphibole-plagioclase thermometry. *Contrib. Mineral. Petrol.* **1994**, *116*, 433–447. [CrossRef]
57. Molina, J.F.; Cambeses, A.; Moreno, J.A.; Morales, I.; Montero, P.; Bea, F. A reassessment of the amphibole-plagioclase NaSi-CaAl Exchange thermometer with applications to igneous and high-grade metamorphic rocks. *Am. Mineral.* **2021**, *106*, 782–800. [CrossRef]
58. Molina, J.F.; Moreno, J.A.; Castro, A.; Rodriguez, C.; Fershtater, G.B. Calcic amphibole thermobarometry in metamorphic and igneous rocks: New calibrations based on plagioclase/amphiboleAl-Si partitioning and amphibole-liquid Mg partitioning. *Lithos* **2015**, *232*, 286–305. [CrossRef]
59. Hammarstrom, J.M.; Zen, E. Aluminium in hornblende: An empirical igneous geobarometer. *Am. Mineral.* **1986**, *71*, 1297–1313.
60. Hollister, L.S.; Grissom, G.C.; Peters, E.K.; Stowell, H.H.; Sisson, V.B. Confirmation of the empirical correlation of Al in hornblende with pressure of solidication of calc-alkaline plutons. *Am. Mineral.* **1987**, *72*, 231–239.
61. Schmidt, M.W. Amphibole composition in tonalite as a function of pressure: An experimental calibration of the Al-in-hornblende barometer. *Contrib. Mineral. Petrol.* **1992**, *110*, 304–310. [CrossRef]
62. Johnson, M.C.; Rutherford, M.J. Experimental calibration of an aluminium-in-hornblende geobarometer applicable to Long Valley caldera (California) volcanic rocks. *Geology* **1989**, *17*, 837–841. [CrossRef]
63. Ridolfi, F.; Renzulli, A. Calcic amphiboles in calc-alkaline and alkaline magmas: Thermobarometric and chemometric empirical equations valid up to 1,130 °C and 2.2 GPa. *Contrib. Mineral. Petrol.* **2012**, *163*, 877–895. [CrossRef]
64. Prinz, M.; Dowty, E.; Keil, K.; Bunch, T.E. Spinel troctolite and anorthosite in Apollo 16 samples. *Science* **1973**, *179*, 74–76. [CrossRef]
65. Bhandari, N.; Srivastava, N. Active Moon: Evidences from Chandrayaan-1 and the proposed Indian missions. *Geosci. Lett.* **2014**, *1*, 11. [CrossRef]
66. Ashwal, L.D. *Anorthosites*; Springer: Berlin/Heidelberg, Germany, 1993; 422p.

67. Kaufmann, F.E.D.; O'Driscoll, B.; Hecht, L. Lateral variations in the Unit 7-8 boundary zone of the Rum Eastern Layered Intrusion, NW Scotland: Implications for the origin and timing of Cr-spinel seam formation. *Contrib. Mineral. Petrol.* **2020**, *175*, 90. [CrossRef]
68. Léger, A.; Ferry, J.M. Highly aluminous hornblende from low-pressure metacarbonates and a preliminary thermodynamic model for the Al content of calcic amphibole. *Am. Mineral.* **1991**, *76*, 1002–1017.
69. Abdu, Y.A.; Hawthorne, F.C. Crystal structure and Mössbauer spectroscopy of tschermakite from the ruby locality at Fiskenaesset, Greenland. *Can. Mineral.* **2009**, *47*, 917–926. [CrossRef]
70. Leake, B.E. On aluminous and edenitic hornblendes. *Mineral. Mag.* **1971**, *38*, 389–407. [CrossRef]
71. Kemp, A.J.; Leake, B.E. Two hydrous-rich aluminous hornblendes. *Mineral. Mag.* **1975**, *40*, 308–311. [CrossRef]
72. Dupuis, C.; Beaudoin, G. Discriminant diagrams for iron oxide trace element fingerprinting of mineral deposit types. *Mineral. Depos.* **2011**, *46*, 319–335. [CrossRef]
73. Oba, T. Phase relationship of $Ca_2Mg_3Al_2Si_6Al_2O_{22}(OH)_2$—$Ca_2Mg_3Fe^{3+}{}_2Si_6Al_2O_{22}(OH)_2$ join at high pressure—The stability of tschermakite. *J. Fac. Sci. Hokkaido Univ.* **1978**, *18*, 339–350.
74. Connolly, J. Multivariable phase diagrams; an algorithm based on generalized thermodynamics. *Am. J. Sci.* **1990**, *290*, 666–718. [CrossRef]
75. Connolly, J.A.D.; Kerrick, D.M. An algorithm and computer program for calculating composition phase diagrams. *CALPHAD* **1987**, *11*, 1–55. [CrossRef]
76. Holland, T.J.B.; Powell, R.A. An internally consistent thermodynamic data set for phases of petrological interest. *J. Metamorph. Petrol.* **1998**, *16*, 309–343. [CrossRef]
77. Holland, T.J.B.; Powell, R.A. Compensated-Redlich-Kwong (CORK) equation for volumes and fugacities of CO_2 and H_2O in the range 1 bar to 50 kbar and 100–1600 °C. *Contrib. Mineral. Petrol.* **1991**, *109*, 265–273. [CrossRef]
78. Evans, B.; Trommsdorff, V. On elongate olivine of metamorphic origin. *Geology* **1974**, *2*, 131–132. [CrossRef]
79. Ohasi, H.; Hariya, Y. Decomposition of $CaFe^{3+}AlSiO_6$ pyroxene at high pressure and low oxygen partial pressure. *J. Jap. Assoc. Mineral. Petrol. Econ. Geol.* **1975**, *70*, 347–351. [CrossRef]
80. Ohasi, H.; Hariya, Y. Phase relation of $CaFeAlSiO_6$ pyroxene at high pressures and temperatures. *J. Jap. Assoc. Mineral. Petrol. Econ. Geol.* **1975**, *70*, 93–95. [CrossRef]
81. Onuma, K. Effect of oxygen fugacity on fassaitic pyroxene. *J. Fac. Sci. Hokkaido Univ.* **1983**, *20*, 185–194.
82. Onuma, K.; Akasaka, M.; Yagi, K. The bearing of the system $CaMgSi_2O_6$-$CaAl_2SiO_6$-$CaFeAlSiO_6$ on fassaitic pyroxene. *Lithos* **1981**, *14*, 173–182. [CrossRef]
83. Lesnov, F.P.; Korolyuk, V.N. Pervye dannye o razpredelenii izomorfnoi primesi zheleza v plagioklazach bazit-giperbazitovych plutonov skladchatych oblastei SSSR (First results of the distribution of isomorphic admixtures of iron in plagioclases of basic-hyperbasic plutons in folded areas of USSR). *Dokl. Akad Nauk SSSR* **1977**, *234*, 922–924.
84. Tegner, C.; Cawthorn, R.G. Iron in plagioclase in the Bushveld and Skaergaard intrusions: Implications for iron contents in evolving basic magmas. *Contrib. Mineral. Petrol.* **2010**, *159*, 719–730. [CrossRef]
85. Jolis, E.M.; Troll, V.R.; Harris, C.; Freda, C.; Gaeta, M.; Orsi, G.; Siebe, C. Skarn xenolith record crustal CO_2 liberation during Pompeii and Pollena eruptions, Vesuvius volcanic system, central Italy. *Chem. Geol.* **2015**, *415*, 17–36. [CrossRef]
86. Matthews, S.J.; Marquillas, R.A.; Kemp, A.J.; Grange, F.K.; Gardeweg, M.C. Active skarn formation beneath Lascar Volcano, northern Chile: A petrographic and geochemical study of xenoliths in eruption products. *J. Metamorph. Geol.* **1996**, *14*, 509–530. [CrossRef]
87. Wenzel, T.; Baumgartner, L.P.; Brügmann, G.E.; Konnikov, E.G.; Kislov, E.V. Partial melting and assimilation of dolomitic xenoliths by mafic magma: The Ioko-Dovyren intrusion (North Baikal region, Russia). *J. Petrol.* **2002**, *43*, 2049–2074. [CrossRef]